5-2021

Investigating Charge Transfer Complexes in Brown Carbon Aerosols

Brianna Peterson

Follow this and additional works at: https://scholarworks.wm.edu/honorstheses

Part of the Analytical Chemistry Commons, and the Physical Chemistry Commons

Investigating Charge Transfer Complexes in Brown Carbon Aerosols

This thesis submitted in partial fulfillment of
the requirements for the degree of Bachelor of Science in Chemistry
from William & Mary

by

Brianna Peterson

Accepted for _____Honors_____

_____Dr. Nathan Kidwell, Director

_____Kristin Wustholz_____ Dr. Kristin Wustholz

_____Rachel O'Brien_____Dr. Rachel O'Brien

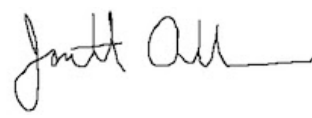_____Dr. Jonathan Allen

Table of Contents

Acknowledgments

I would like to thank Professor Kidwell for allowing me to join his lab and guiding me through the research process in this project, as well as, answering all my questions. It has been an absolute joy to learn so many things that I never dreamed of doing. I would also like to thank my lab mate and computational mother, Emily, for teaching me everything I know about the HPC; David and Chris for help on my experiment at the sacrifice of collecting their own data; and Megan, for all the lab company. Finally, a thanks must go to my family and friends who have supported me through everything, including mouth pipetting sea star larvae prior to my time in Kidwell lab.

List of Tables

List of Figures

Abstract

Aerosols are suspensions of particles in the air, commonly seen as dust or fog in the atmosphere. Brown carbon is a particular classification of carbonaceous atmospheric aerosol that increases in absorption from the visible to ultraviolet region, making it important for radiative forcing models. Elucidating the structures of brown carbon chromophores has been difficult as brown carbon is a broad category and the chromophore type can change depending on emission source, temperature, humidity, and season. Twisted intramolecular charge transfer (TICT) molecules have been identified as potential brown carbon chromophores. TICT molecules are those that allow charge transfer to occur between portions of the same molecule when that molecule is in a particular twisted conformation upon photoexcitation. Therefore, 1-phenylpyrrole (1PhPy) was examined using both resonant two-photon ionization (R2PI) spectroscopy and computational methods as a potential TICT molecule and brown carbon chromophore. These methods were carried out for both 1PhPy as the bare chromophore in the gas phase and with one water-molecule complexation, 1PhPy + 1H_2O. Additional calculations were carried out for 1PhPy + 2H_2O and 1PhPy + 3H_2O. Both the bare chromophore and water clusters were shown to become more twisted in their excited state compared to their ground state analogue. Furthermore, the addition of water solvent decreased the energetic barrier to twisting, facilitating charge transfer. The effect of the water solvation on charge transfer is important for considering how chromophores will behave in the aerosol condensed phase. The presence of a TICT state shifts the absorbance of brown carbon chromophores to overlap more strongly with the solar flux. Developing a molecular-level understanding of the photophysics of brown carbon chromophores with and without water solvent will lead to greater understanding of the outcomes from aerosol solar absorption.

Chapter 1: Introduction

1.1 Aerosols and Brown Carbon

Aerosols are suspensions of fine solid materials or liquid droplets in air or another gas (Lary et al., 1997). In typical day-to-day life, people see atmospheric aerosols in the form of dust or fog. The incomplete combustion of fossil fuels is another pathway via which aerosols can be produced. Particulate matter or aerosols formed from incomplete combustion of fossil fuels contain high amounts of carbon, so they are often referred to as carbonaceous aerosols (Chung and Seinfeld, 2002). Soot from fires is an example of a carbonaceous aerosol.

The category of carbonaceous aerosols can be broken down even further. Traditionally, they were broken down into black carbon and organic carbon (Chung and Seinfield, 2002) Across the literature, black carbon may refer to the particles as a whole or to the specific light-absorbing portion of the particle in question. Black carbon is responsible for much of the radiative forcing in the atmosphere and is considered a major pollutant. The light absorption of black carbon does not vary greatly with wavelength (Bergstrom et al., 2002).

Organic carbon is much harder to categorize as it encompasses a wide group covering varying compounds each with its own unique properties that typically absorb light more strongly in the UV region (Turpin et al., 2000) This wide array of properties makes it difficult to both measure and characterize. Typical organic carbon sampling errors include volatilization of compounds from the sample container or even interactions with the organic sample and the container it is in. Since black carbon is such a strong solar absorber and organic carbon is difficult to accurately measure, oftentimes black carbon absorption will be measured and the measure of organic carbon will be calculated as the difference between black carbon absorption and total aerosol amount.

This classification of aerosols into either black carbon or organic carbon was improved upon by the addition of a group called 'brown carbon' (Andreae and Gelencsér, 2006). Prior to this, black carbon was used as a blanket term to define all forms of light-absorbing carbonaceous aerosols. While black carbon absorption does not vary with wavelength, the absorption of brown carbon is highly dependent on wavelength. The absorption spectrum of brown carbon is characterized by a smooth increase in absorption from the visible to ultraviolet range.

One way the different types of aerosols can be classified is by an optical property known as the absorption Ångström exponent (AAE) (Liu et al., 2018). This is a property of an aerosol that characterizes the aerosol's absorption and how it changes across wavelength. It can be calculated from the wavelength (λ), aerosol absorption coefficient (C_{abs}), and a wavelength-independent constant (C_0).

$$\ln(C_{abs}(\lambda)) = \ln(C_0) - AAE \ln(\lambda)$$

The AAE of an aerosol can be impacted by its particle size, shape, and composition. Black carbon has an AAE measured about equal to one, while brown carbon and organic carbon will have an AEE greater than one (Desyaterik et al., 2013). The ranges in AAE may be due to different chemical compositions of brown carbon chromophores, the light-absorbing molecules within brown carbon aerosols, indicating that the chromophore composition varies depending on the source of the brown carbon (Bergstrom et al., 2007).

Brown carbon can come from different emission sources and have different optical properties depending on the emission source (Laskin et al., 2015). In a study looking at wavelength-dependent absorption in different aerosol types, researchers found that savanna fires

and firewood smoke particles contained more brown carbon (Kirchstetter et al., 2004). That is, absorption increased as wavelength decreased. Aerosol measurements taken adjacent to runways did not have this same absorption pattern indicating that they are made up of a higher amount of black carbon, which does not change absorbance across wavelengths. It has also been found that aerosols produced by biomass burning contain more brown carbon than biogenic particles (Rizzo et al., 2011). This trend is supported by other studies as well. A study conducted in Switzerland demonstrated that traffic pollution contains higher amounts of black carbon, while wood-burning produces more brown carbon aerosols (Sandradewi et al., 2008). Atmospheric humic-like substances (HULIS) have been noted as important components in the formation of brown carbon (Mukai and Ambe, 1986). In atmospheric particulate matter samples, humic acid-like structures were extracted. Structures for HULIS include compounds with polycyclic ring structures and hydrocarbon chains. HULIS also absorb more strongly at shorter wavelengths, a descriptor of brown carbon (Dinar et al., 2008).

Combustion temperature and moisture content also greatly impact the absorption properties of different brown carbon sources (Laskin et al., 2015). In a study varying the temperature of wood combustion, increased absorption was observed with an increase in temperature (Chen and Bond, 2010). This suggests that increased temperatures could allow for further reactions between particles, allowing for the creation of more high-absorbing brown carbon chromophores.

Brown carbon has been measured in cloud water as well, suggesting that certain brown carbon chromophores do have the ability to interact with water molecules and at least some are water-soluble (Desyaterik et al., 2013). It has been further observed that in high relative humidity tarballs (a type of brown carbon aerosol) can absorb water and may be able to serve as nucleation sites for clouds (Hand et al., 2005; Laskin et al., 2015). Water solubility may help further elucidate

structures of potential brown carbon chromophores. Research has found that the portion of organic carbon that can be extracted with methanol absorbs more at shorter wavelengths than the portion that can be extracted by water (Chen and Bond, 2010; Zhang et al., 2013)

Furthermore, temporal variations in brown carbon concentrations throughout the day also suggest secondary reactions are taking place in the atmosphere (Zhong and Jang, 2014). In analyzing aerosol absorption over time, absorption first increased, then decreased. This indicates that secondary reactions promoted the formation of more light-absorbing chromophores, which were then overall bleached as time progressed. There is even seasonal variation in brown carbon absorption as reported by Chen et al., 2018. They discovered that in samples taken in Nanjing, China, winter had the highest amount of absorption at shorter wavelengths when compared to other months. The absorption angstrom coefficient varied seasonally as well, suggesting that chromophore composition changed across the seasons. In addition, the ratio of secondary organic carbon to primary organic carbon was greater than one, supporting the idea that secondary reactions can promote the formation of more light-absorbing chromophores.

1.2 The Impact of Aerosols on Radiative Forcing

Classifying carbonaceous aerosols matters because aerosols play a large role when it comes to radiative forcing of the atmosphere and are important in predictive models of climate and radiative forcing (Chung and Seinfeld, 2002; Zhang et al, 2009). Radiative forcing is the difference between the solar radiation absorbed by the Earth and the heat emitted back into space (Haywood and Boucher, 2000) When more solar energy is absorbed than is emitted, this is positive radiative forcing and results in net warming. Aerosols can affect the radiative forcing of the atmosphere in two ways. First, aerosols can serve as cloud nucleation sites, stimulating the production of more

clouds in the atmosphere. More clouds would, in turn, increase the Earth's albedo and result in negative radiative forcing. Second, as we have previously described with black and brown carbon, aerosols can absorb more radiation and result in an overall positive radiative forcing effect. These diametrically opposed aerosol effects can make creating climate models difficult, especially as aerosol types are described and classified. Previously, black carbon was thought to primarily absorb radiation, while organic aerosols were more reflective (Zhang et al., 2017). However, with the further observation and description of brown carbon aerosols, some organic carbon may be contributing to light absorption as well. In fact, some estimates put brown carbon as being responsible for up to 24% of radiative forcing that was previously thought to be from black carbon (Lin et al., 2014). As brown carbon absorption is strongly wavelength-dependent, this estimate could vastly change climate models.

In addition to scattering or absorbing radiation by itself, further reactions of aerosols and the atmosphere can occur, resulting in even more absorbing matter (Kampf et al., 2016). For example, biogenic precursors, such as limonene or pinene, have been found to absorb light like brown carbon after being reduced by atmospheric ozone and aged by NH_3 or NH_4^+ (Updyke et al., 2012). Between contrasting effects and secondary reactions, the uncertainty in the effect aerosols are having overall on our atmosphere is something that needs to be studied more. This can be done by improving our understanding of aerosol optical properties.

1.3 Structure of Brown Carbon Chromophores

Our understanding of aerosol optical properties can be improved by directing more attention towards studying brown carbon chromophores. Recall that chromophores are the portions of an aerosol responsible for its light-absorbing properties. Determining the structure of brown

carbon chromophores is a difficult task due to the necessary analytical techniques such as mass spectrometry that are needed (Laskin et al., 2015). However, there are some molecular characteristics that have been suggested to make up the structure of brown carbon chromophores.

In order for absorption at ultraviolet and visible wavelengths (100-700 nm) to occur, there is often a $\pi \rightarrow \pi^*$ or n $\rightarrow \pi^*$ electronic transition that occurs (Sun et al., 2007). This means that the brown carbon chromophores must be capable of making these transitions. A $\pi \rightarrow \pi^*$ transition would require a chromophore with double bonds, while an n $\rightarrow \pi^*$ transition requires a nonbonding pair of electrons. Since a majority of sunlight is radiated in ultraviolet and visible wavelengths, being able to absorb in this range is critical for any potential brown carbon chromophore. Conjugated molecules containing oxygen or nitrogen species would fit this characterization due to the double-bonded nature of conjugated systems, as well as, the lone pairs the oxygen and nitrogen could contribute.

Pyrrole and its derivatives fulfill many of the common structural motifs identified across brown carbon chromophores (Laskin et al., 2015). Using gas chromatography, 2-methyl pyrrole was observed as an intermediate step in the browning of 4-oxopentanal reacted with ammonium sulfate (Aiona et al., 2017). This could mean that pyrrole derivatives are important in further atmospheric reactions that produce brown carbon chromophores. In addition, larger pyrrole frameworks created by the Paal-Knorr synthesis could contain enough conjugation to promote a larger red-shift absorption in the visible region (Kampf et al., 2016). The Paal-Knorr synthesis involves reactions of 1,4 dicarbonyl containing compounds with excess of ammonia or a primary amine to generate pyrrole or one of its derivatives (Amarnath et al., 1991). 1,4 dicarbonyls are found in important atmospheric molecules such as 4-oxopentanal examined by Aiona et al. (2017)

and ketolimonoaldehyde (KLA) which is a secondary organic aerosol (SOA) produced from limonene, a biogenic aerosol (Nguyen et al., 2013).

There is also supporting evidence that charge transfer (CT) complexes, either intermolecular or intramolecular might be responsible for a set of brown carbon chromophores (Phillips and Smith, 2014). A charge-transfer complex is one where electronic charge is transferred from a donor to an acceptor upon excitation of molecules. When the donor and acceptor are on two different molecules, the process is often referred to as intermolecular charge transfer. When the donor and acceptor exist on the same molecule, it is referred to as intramolecular charge transfer. If the donor and acceptor moieties are able to undergo large amplitude motion, then a twisted intramolecular charge transfer (TICT) state can be reached during photoexcitation (Sasaki et al., 2016). TICT molecules are able to adopt a twisted (perpendicular) conformation because the electron transfer during photoexcitation makes the 90˚ conformer the lowest-energy configuration. Polar environments such as water solvation can also induce TICT states because the polar solvent is able to stabilize the molecule and lower the energy of the TICT configuration. Therefore, TICT states can affect the UV/Vis absorption by creating a red-shift to longer wavelengths in the visible region where the solar flux is high.

Phillips and Smith (2014) observed that when extracted aerosol solutions and fulvic acid solutions were reduced with $NaBH_4$, they lost absorption, especially at longer wavelengths. The $NaBH_4$ reduced the carbonyl groups present on aldehydes and ketones, which are potential electron acceptors in CT complexes. This indicates that a least a portion of the aerosol absorption in the study was due to CT.

Energetics are incredibly important to understanding TICT molecules and whether or not a molecule could have a TICT state. As mentioned previously, in order to achieve a TICT state,

the perpendicular orientation of a molecule must be the lowest-energy configuration to allow charge transfer to occur most efficiently. When discussing molecular orientation in this case, the dihedral angle of a molecule is the best indicator of a planar vs. perpendicular structure (Figure 1). In a two-fold rotation scheme, this makes dihedral angles equal to 0˚ for a planar molecule and +/- 90˚ for a perpendicular molecule. Molecules can fall anywhere along that range from nearly planar to nearly perpendicular. The energy required for molecules to twist from their optimized geometry to become more planar or perpendicular will be referred to as the barrier to planarity (ΔE_0) and the barrier to perpendicularity (ΔE_{90}), respectively. In other words, these are the energetic barriers a molecule must climb in order for internal rotation to occur. Further examining the energetics surrounding TICT states and their behavior in solvents is important to better understanding their behavior in the atmosphere and importance in light absorption.

Energetic barrier

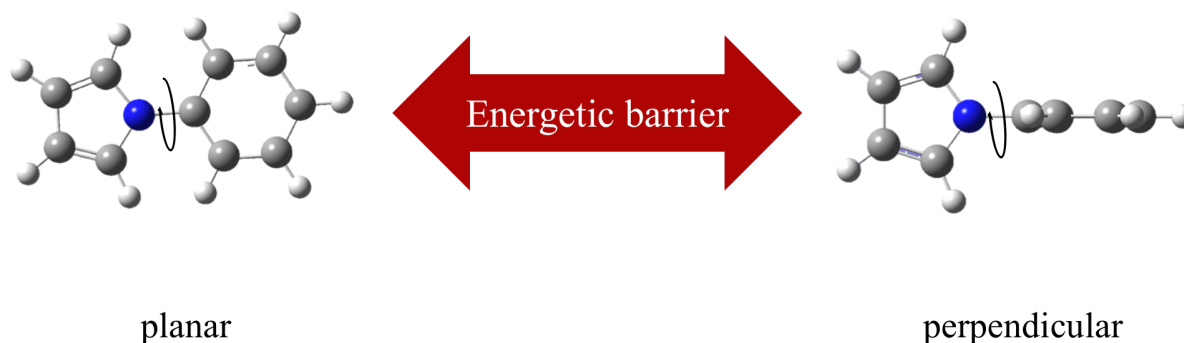planar   perpendicular

Figure 1: 1-Phenylpyrrole showed in the planar (left) and perpendicular (right) conformations with respects to the dihedral between the pyrrole and phenyl rings indicated by the black arrow. The red arrow represents the energy barriers that must be overcome to go between the two conformers.

1.4 1-Phenylpyrrole as a Twisted Intramolecular Charge Transfer Molecule and Brown Carbon Chromophore

Phenylpyrrole (1PhPy) shown in Figure 1 is a potential brown carbon chromophore and a disputed TICT molecule in the literature. In the case of 1PhPy, the pyrrole group becomes the electron donor and the phenyl group becomes the electron acceptor upon excitation. Sarkar and Chakravorti (1995) reported that 1PhPy in a mixture of ethanol and water produced a fluorescence band attributed to the TICT state. Experimental research by Okuyama et al. in 1998 indicated the ground state of isolated 1PhPy is optimized with a 38.7° dihedral angle, while the excited state had a dihedral of 19.8°. As a result, the authors determined that the excited state was more planar than the ground state. In addition, they used the vibronic transitions observed in the spectra to determine torsional potentials for 1PhPy and fit the data with a Franck-Condon simulation analysis. In the excited state, it was found that ΔE_{90} was a factor of ten greater than the value of ΔE_0 (Table 1). Since the barrier to perpendicularity was much higher than the barrier to planarity, Okuyama et al. concluded that 1PhPy became rigid to twisting in the excited state and was therefore not a TICT molecule.

Proppe et al., (2000) followed up the Okuyama et al. study with theoretical calculations using CASSCF/CASPT2 level of theory. This is an *ab initio* and computationally intensive method typically associated with a high level of accuracy. They obtained similar dihedral angle results as the experimental data (Table 1) but differed in the calculations of ΔE_0 and ΔE_{90}. For the ground state, Okuyama et al. determined experimentally that $\Delta E_0 = 457$ cm^{-1}, which is smaller than the $\Delta E_{90} = 758$ cm^{-1}. However, the reverse was calculated for the ground state from Proppe et al. ($\Delta E_0 = 813$ cm^{-1}, $\Delta E_{90} = 518$ cm^{-1}). The trend for the excited state calculations from Proppe did follow the experimentally derived values for ΔE_0 and ΔE_{90} from Okuyama, with ΔE_{90} being much larger and therefore a barrier to twisting occurring in the photoexcited state (excited state: $\Delta E_0 = 431$,

ΔE_{90} = 2,236; Proppe et al., 2000). However, despite obtaining similar results in the excited state to Okuyama et al., Proppe argued that 1PhPy is still a TICT molecule and that when placed in a polar solvent, such as acetonitrile, the barrier to perpendicularity was reduced. They also concluded that the switch in ΔE_0 and ΔE_{90} for the ground state was due to underestimations by the experimental values based on similar results seen in biphenyl (Rubio et al., 1995; Tsuzuki & Tanabe, 1991).

In 2010, Thomas et al. continued the debate with a combined experimental/theoretical study on 1PhPy using jet-cooled molecules with high-resolution spectroscopy combined with the M05-2X/6-31G level of theory. Their study found that the transition dipole moment upon excitation was approximately 2.5 Debye (D), indicating a large moment in charge upon excitation of the molecule and supporting the idea that 1PhPy is a TICT molecule. This is contradicted somewhat in their theoretical results. The theoretical calculations correlate to those experimentally derived by Okuyama et al. in terms of the excited state being more planar than the ground state with a higher barrier to perpendicularity. The ground state data matched as well, with the barrier to planarity being lower than the barrier to perpendicularity. This is again unlike what was seen in Proppe et al.

The controversy in the literature demonstrates the importance of polar solvents when it comes to identifying TICT molecules. The three studies mentioned (Okuyama et al.; Proppe et al.; Thomas et al.) focused on 1PhPy in isolated gas-phase conditions without any solvent interactions. Proppe et al. does include a portion discussing the effect of acetonitrile on the 1PhPy, suggesting that it does allow for the barrier to perpendicularity to be lowered in the excited state so that 1PhPy would be flexible to twisting. Furthermore, Schweke et al. (2005) generated 1PhPy with

acetonitrile clusters in an argon matrix and determined that 1PhPy behaved more like a TICT

molecule as a complex rather than in isolated form.

Table 1: Summary of gas-phase values for 1PhPy as found in the literature.

Author	Value	S_0 Dihedral	S_1 Dihedral	Ground ΔE_0 (cm^{-1})	Ground ΔE_{90} (cm^{-1})	Excited ΔE_0 (cm^{-1})	Excited ΔE_{90} (cm^{-1})
Okuyama et al., 1998	Experimental	38.7˚	19.8˚	457	758	105	1526
Proppe et al., 2000	Theoretical	41.1˚	25.5˚	813	518	431.34	2,236.12
Thomas et al., 2010	Theoretical	37.3˚	≈ 20˚	634	824	164	Above 900

The answer to the question of whether or not 1PhPy should be considered a TICT molecule

is the focus of this thesis. As nitrogen-containing heterocycles and TICT molecules have some

support as brown carbon chromophores, this warrants further investigation on 1PhPy. This is

particularly true for examining the behavior of 1PhPy in polar environments to determine if solvent

interactions will lower the excited state barrier to perpendicularity and allow the molecule to twist

to a more preferred TICT configuration. With this in mind, the following sections will describe

the experimental and theoretical approaches to exploring this problem, using water as a polar

solvent given the importance of water in aerosol condensed-phase environments and atmospheric

conditions.

Chapter 2: Theoretical and Experimental Methods

2.1 Theoretical Methods

Computational chemistry is devoted to using theoretical methods to solve chemical problems that complement insights revealed with experimental methods. It can also aid in experimental research by providing predictions of observables obtained in the laboratory. This project makes use of computational chemistry to complement our experimental studies and for its predictive power. For this project, the chemical structure of 1-phenylpyrrole (1PhPy) was constructed utilizing GaussView 6.0.16. Different proposed conformers of 1PhPy were created by rotating the molecule's dihedral bond. To begin, ground-state vibrational frequency and optimization calculations were carried out using the density functional theory (DFT) ωB97XD level of theory with the 6-311G++(d,p) basis set.

DFT is a computational method that uses electron density as compared to other methods such as the Hartree-Fock method, which uses wave functions to describe chemical systems (Baseden and Tye, 2014). This allows for fairly accurate of calculations but at a lower computational cost as compared to Hartree-Fock and post Hartree-Fock methods. DFT uses functionals to describe the properties of a system and in the case of this project, the functional used is ωB97XD (Chai and Head-Gordon, 2008; Chai and Head-Gordon, 2008). This is a hybrid functional that combines portions of wave function theory (WFT) and DFT. The ωB97XD functional is a good functional to use because it is good at considering dispersive interactions between molecules (in this case 1PhPy and water), as well as, increasing long-range exact exchange, which removes long-range self-interactions. This allows for better calculations for charge transfer states when compared to other functionals (such as B3LYP), that do not contain this long-range optimization. Recall that a charge transfer state occurs when an electron is

transferred from a donor to an acceptor (Sasaki et al., 2016). In the case of these studies, we are looking at intramolecular charge transfer meaning the donor and acceptor groups are contained within the same molecule.

The 6-311G++(d,p) basis set provides good results when combined with DFT (Krishnan et al., 1980). A basis set is the approximate representation of the atomic orbitals of the molecule that will be used in the calculation. The larger the basis set, the more accurate results will be, but also at the cost of computational time. The basis set 6-311G++(d,p) contains split valence, polarized, and diffused elements. Split valence basis sets include additional atomic orbitals for each atom. For example in carbon, a minimal basis set would only contain one set of atomic orbitals that describe the atom. A split valence basis set contains multiple (depending on the type) atomic orbitals to describe the same atom. This allows for a better approximation of the molecular orbitals. In 6-311G, there are six Gaussian-type orbitals used to describe the core electrons of each atom, and then three different descriptors for the valence electrons of various sizes. The (d,p) addition to the basis set makes it polarized by adding in atomic orbitals with higher angular momentum than what the atom is typically associated with having. For example, adding a p-orbital to a hydrogen atom allows a more flexible basis set equipped to deal with chemical bonding. The ++ makes the basis set diffuse, allowing it to better describe systems where the electrons may be further away from the nucleus, such as in an excited state. All of these things combined make 6-311G++(d,p) a robust basis set choice for the calculations required in this project.

Following optimization in the ground electronic state, the output files were analyzed and the ground state energy (converted to relative wavenumbers, cm^{-1}) and dihedral angle were recorded. All vibrational frequencies of each calculation were also examined to ensure that true minima (having real vibrational frequencies) were being recorded rather than transition states. The

level of theory changed for the excited state, where we used the TD-SCF DFT ωB97XD method with the 6-311G++(d,p) basis set. TD-SCF stands for time-dependent self-consistent field and helps DFT to more accurately predict excited-state properties (van Mourik et al., 2014). The optimized ground state geometry was used as the starting point for excited state optimization. Following optimization of the excited state, the output files were again analyzed, and the excited-state energy was recorded, as well as the dihedral angle and the predicted UV/Vis absorption for the first excited state.

The next set of calculations involved the addition of 1, 2, and 3 water molecules to the bare 1PhPy using the software ABCluster (Zhang and Dolg, 2015). This is a program that makes use of the artificial bee colony algorithm, meant to simulate how bees communicate with each other to find nectar. The configurational search algorithm allows the formation of water clusters and the analysis of different isomers to find the lowest-energy configurations while minimizing the possibility that the calculation will get trapped in a local minima energy well (Zhang and Dolg, 2015). The geometry optimization and vibrational frequency calculations including clusters with water were performed at the same level of theory as the 1PhPy ground state calculations. This generated 200 possible conformers that were ordered by relative energy. The lowest energy conformer's ground state energy and dihedral angle were recorded. Then, excited-state calculations were completed for the lowest energy water cluster isomers, where the excited state energy, dihedral angle, and predicted UV/Vis absorption peak were recorded.

In order to visualize the types of transitions occurring upon electronic excitation, vertical excitation calculations were carried out at the same level of excited state theory on the optimized ground state geometries. The highest occupied molecular orbital (HOMO), lowest unoccupied molecular orbital (LUMO), wavelength, oscillator strength, and energy associated with each

excited state transition were recorded. The molecular orbitals for each HOMO and LUMO were pictorially represented to understand the nature of the electronic transitions and the transition type ($\pi \rightarrow \pi^*$, etc.) was recorded.

To generate theoretical potential energy surfaces for the 1PhPy bare chromophore, along with 1, 2, and 3 water molecules in both the ground and excited state, dihedral scan calculations were also completed within Gaussian. This was done at the same level of theory as listed before (excluding 1PhPy + $3H_2O$ excited state which was run with a 6-31G ++ (d,p) basis set due to computational costs), changed appropriately for either ground or excited state. Here, the dihedral angle was scanned at 10 degree increments for 40 total steps (Figure 2). Once the calculation finished, the energy values were converted to relative energy in wavenumbers and then plotted against dihedral angle. This allowed prediction of the barriers to planarity and perpendicularity within each molecule to better understand its behavior in the ground and excited state.
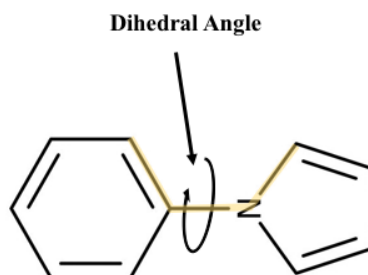

Figure 2: The structure of 1PhPy with the dihedral angle of interest highlighted.

2.2 Introduction to Experimental Techniques

2.2.1 Supersonic Jet Expansion

A supersonic jet expansion was used to obtain the spectroscopic data of isolated, gas-phase molecules without the interference from other species present in the expansion. As illustrated in Figure 3, the gas molecules are seeded with a monatomic carrier gas, such as helium or argon, and then injected into a high-vacuum chamber from a pulse valve with a small opening (Smalley et al., 1976). This opening is larger than the mean free path of the molecules, so as the gas molecules travel out of the reservoir towards a lower pressure area downstream, they collide with the inert carrier gas. These collisions change the random molecular motion into a focused mass flow, which in turn causes a decrease in internal energy for the molecule and/or molecular complex of interest. The increase in the velocity of the molecules and decrease in the internal energy causes the velocity distribution to shift towards higher velocities and narrow in distribution. Translational cooling will occur, followed by rotational cooling, and then to a slightly lesser extent, vibrational cooling. Therefore, supersonic jet expansion allows molecules and molecular complexes to cool to temperatures of a few Kelvin without condensing them to the liquid or solid phase (Hayes and Small. 1983). Furthermore, as a result of the supersonic jet expansion reducing the molecule's internal energy, the spectral lines are narrow (*fwhm* ~ 1-3 cm^{-1}), facilitating accurate assignments.
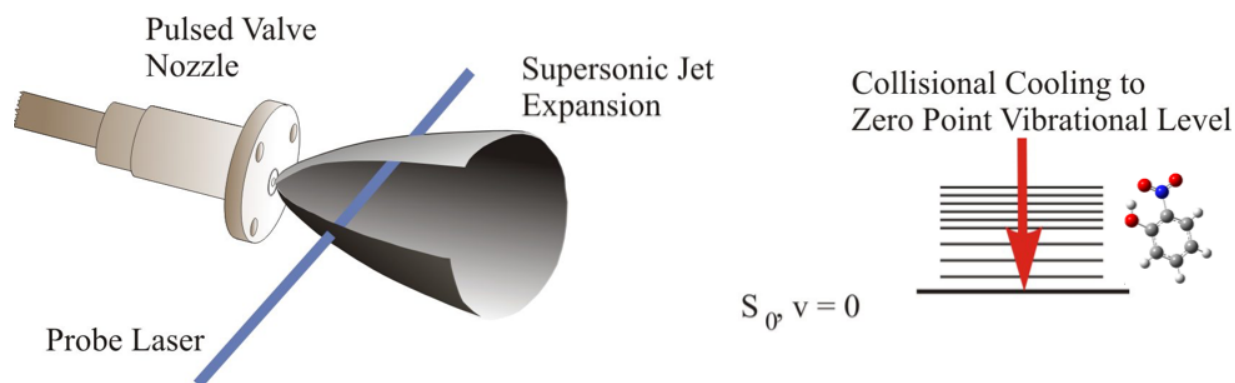

Figure 3: An overview of supersonic jet expansion. On the left, the pulse valve is shown with a probe laser used to interrogate the jet-cooled molecules. The diagram on the right is showing the adiabatic cooling that occurs in the translational, rotational and vibrational states of a molecule.

2.2.2 Resonant Two-Photon Ionization (R2PI)

As Figure 4 shows, resonant two-photon ionization (R2PI) uses a probe laser to excite the molecule of interest that has been cooled in a supersonic jet expansion to a target electronic excited state (Zwier, 2006). Then, another photon of the same wavelength ionizes the population of molecules in the excited electronic state – either from the same laser if the ionization energy required is low enough or from another higher-powered laser at shorter wavelengths. From combining R2PI with a time-of-flight (TOF) mass spectrometer, a mass-resolved electronic spectrum can be obtained containing all the various conformers of the molecule or complex by scanning the probe laser wavelength and monitoring the mass channel ion signal.
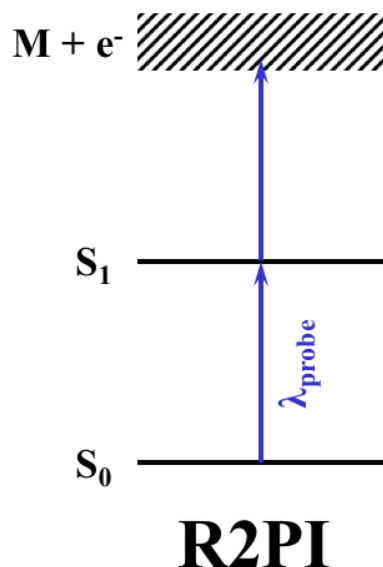

Figure 4: A diagram showing the electronic transition of a molecule or complex from ground to excited state using one photon, then from excited state to the ionization continuum using a second photon.

2.3 Experimental Methods

A sample of solid 1-phenylpyrrole (1PhPy) was placed in the sample container and heated to 40°C to obtain sufficient vapor pressure. The sample was jet-cooled in a supersonic jet expansion as described above using helium (He) gas for the spectroscopy measurements of 1PhPy with and without water complexation due to its better cooling efficiency. Water clusters were created by building a water line and connecting it to the chamber (Figure 5). Using a mass flow meter (Teledyne Hastings), the 1PhPy sample gas flow, water gas flow, and total gas flow were monitored. As can be observed in Figure 5, the main He gas line is split into two gas channels - pure He gas and a channel containing the water sample. Water clusters were generated by opening the gas shutoff valve to the water sample, and the gas flow was fine-tuned with a needle valve to optimize experimental conditions to produce target water cluster sizes. The pure He gas channel and water channel re-converge, where the gas entrains the 1PhPy vapor in the pulsed supersonic jet expansion to generate 1PhPy + nH_2O clusters. The gas line can be heated to create larger clusters, and the total flow is monitored to determine number densities.
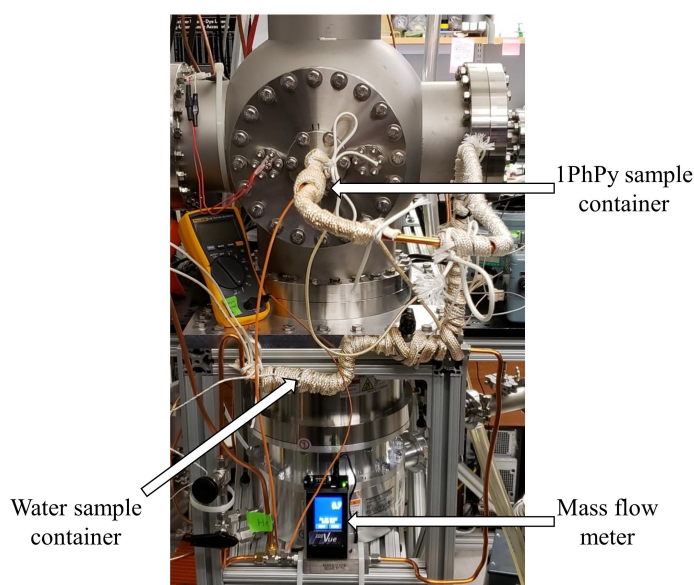
Figure 5: The experimental setup of the water line and sample containers in the lab. The water sample container, 1PhPy sample container, and flow meter are all indicated on the figure.

To ensure that only the coldest molecules were reaching the detector, a skimmer was installed in the chamber (Figure 6). The skimmer removes the outer portion of the supersonic jet expansion which contains the warmest portion of the gas-phase molecules (Campargue, 1984). Therefore, the population subset with the lowest internal energy was selected to be probed using R2PI spectroscopy.
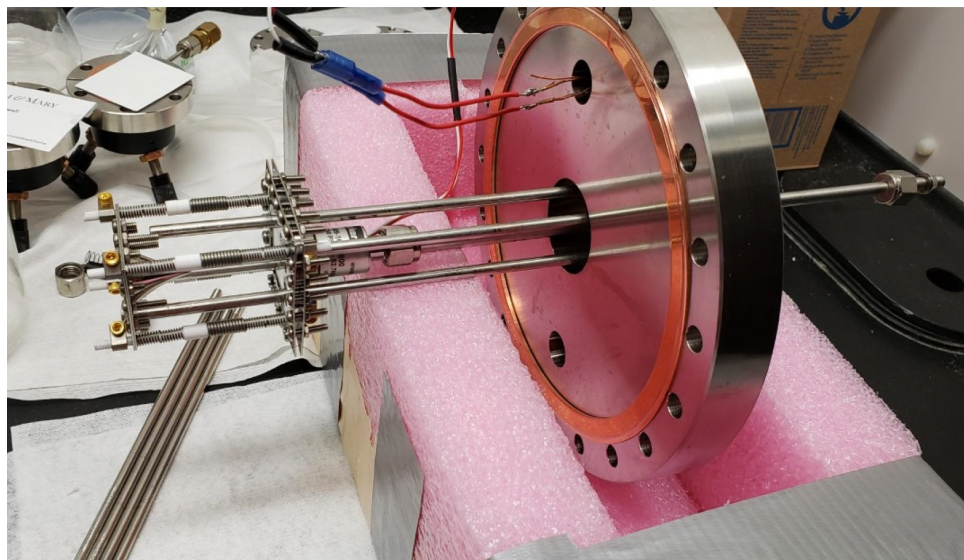
Figure 6: The skimmer installed in the experimental setup.

Using a Nd:YAG-pumped dye laser (NarrowScan) with Rhodamine 6G dye, a mass spectrum was first taken of the sample using the time of flight (TOF) mass spectrometer. Then, the mass ion signal could be selected and monitored to obtain the electronic spectrum using R2PI. R2PI spectra were collected by scanning the region from 35000 to 36500 cm^{-1} with the use of an Inrad Autotracker III with BBO frequency-doubling crystals to obtain the UV radiation. Scans were taken multiple times and then averaged together. For the 1PhPy:H$_2$O cluster, the dye was changed to a mix with Rhodamine B, to enable scanning the wavelength to lower energy. A TOF

mass spectrum was taken and the peak of interest was selected again. Scans were taken multiple times and averaged together.

A UV/Vis was taken of 1PhPy dissolved in water and acetonitrile using a Perkin Elmer Lambda 35 UV/Vis spectrophotometer. Samples were diluted until a reasonable amount of signal was seen from the instrument.

Chapter 3: Results

3.1 Theoretical Results

3.1.1 Bare Chromophore

Figure 7 shows the calculated ground and excited state geometries for 1PhPy. Only one conformer was found in the ground state with a CN-CC dihedral angle of 40.2˚. This is a somewhat twisted configuration between complete planarity (0˚) and complete perpendicularity (90˚). The excited state calculations optimized to two different minima, but the lowest-energy excited state conformer has a dihedral angle of 67.9 ˚ that is closer to perpendicularity. Compared to the ground state structure, a bent structure is observed between the pyrrole and phenyl rings in the excited state. The zero-point energy gap between the ground and excited state is 38,878 cm^{-1} (Table 2). Analyzing the molecular orbitals between the relevant ground and excited states reveals that the electronic transition is π-π* in nature from the pyrrole ring to the phenyl ring.
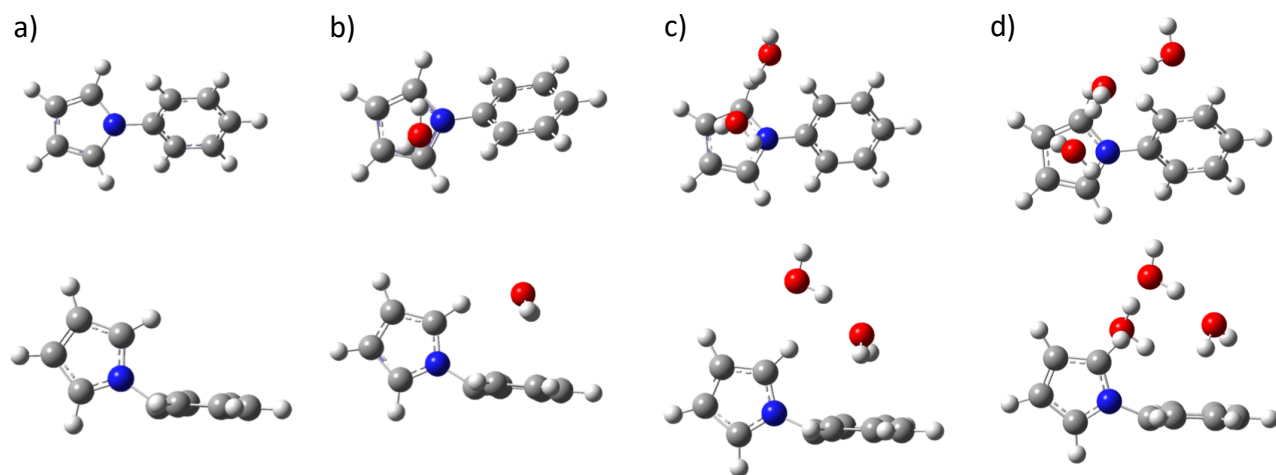

Figure 7: The optimized geometry of a) 1PhPy, b) 1PhPy + 1H$_2$O, c) 1PhPy + 2H$_2$O, and d) 1PhPy + 3H$_2$O in its ground (top) and excited (bottom) state.

Table 2: The calculated ground and excited state energies and dihedral angles for 1PhPy.

	Energy relative to ground state (cm^{-1})	Dihedral Angle (°)
Ground	0	40.2
Excited	38,878	67.9

3.1.2 Addition of Water Molecules

Table 3 summarizes the relative energy between the ground and excited electronic states for 1PhPy + $1H_2O$, 1PhPy + $2H_2O$, and 1PhPy + $3H_2O$. The optimized geometry for each structure is in Figure 7. Recall that water clusters were produced by ABCluster, which generated 200 arrangements of the 1PhPy and water. Out of those 200 conformers, the lowest energy one was chosen and optimized. In general, the adiabatic energy gap is predicted to increase as the number of water molecules increases, although the cluster with two water molecules had a smaller energy difference. However, all water cluster predicted energies are red-shifted with respect to the 1PhPy bare chromophore. Furthermore, the dihedral angles changed from a semi-twisted conformation in the ground state (-54.2°, 40.1°, and 44.5°) to a more twisted conformation in the excited state (70.3°, 74.1°, 91.2°). Likewise, the nature of the first excited electronic transition is π-π*.

Table 3: The calculated ground state energy and dihedral angle for 1PhPy + nH_2O (n=1-3).

	1PhPy + $1H_2O$	1PhPy + $2H_2O$	1PhPy + $3H_2O$
Excited State Relative Energy (cm^{-1})	36,616	36,340	38,107
Ground State Dihedral (°)	-54.2	40.1	44.5
Excited State Dihedral (°)	70.3	74.1	91.2

3.1.3 Potential Energy Scans

As observed in Figure 8, the ground state of 1PhPy has clear barriers to planarity (ΔE_0; dihedral angle=0°) and perpendicularity (ΔE_{90}; dihedral angle=90°) seen by the repetition of two transition state geometries across the scan. Different geometries are overlayed on the potential energy surface and all energy values are reported with respect to the minimum energy conformer. The calculated ΔE_0 is equal to 652 cm^{-1} and ΔE_{90} is equal to 579 cm^{-1}, making the difference between the two approximately 70 cm^{-1} where ΔE_{90} is smaller.
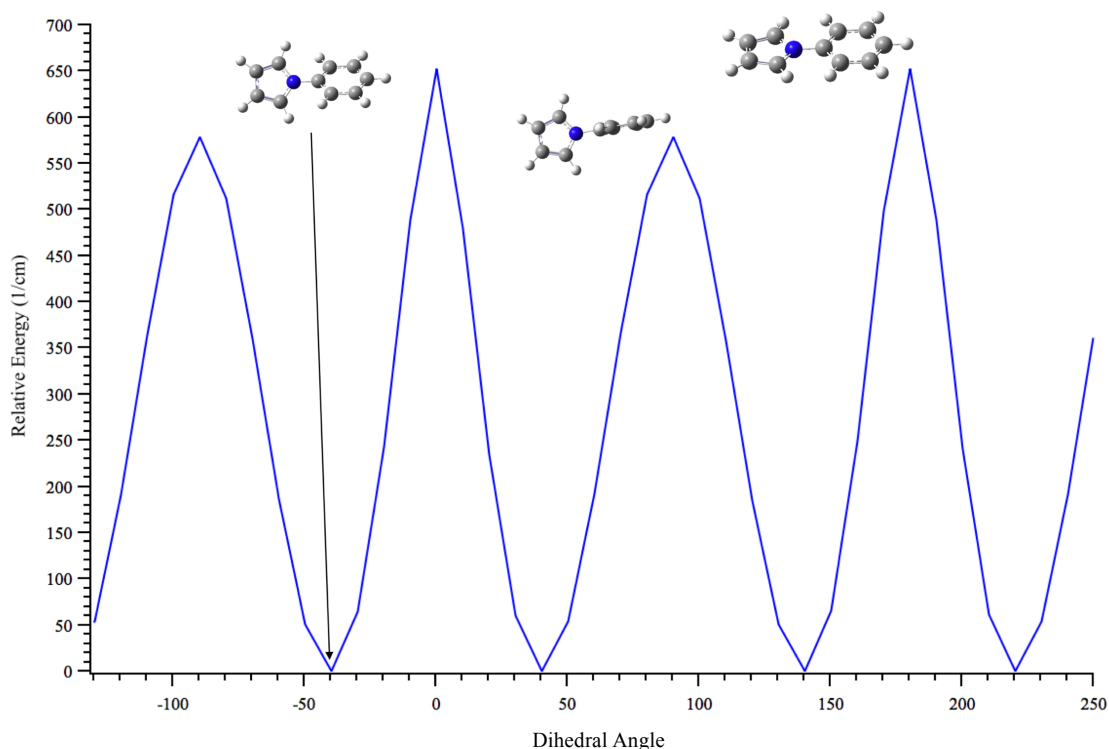
Figure 8: The 1PhPy bare chromophore ground state potential energy surface. The structure at -40˚, 90˚, and 180˚ are shown representing the geometry at the optimized state, ΔE_{90}, and ΔE_0, respectively.

For the dihedral scan in the excited state (Figure 9), the two-fold pattern of transition state energies is not seen as in the ground state, and the barriers to planarity and perpendicularity are also changed. The barrier to planarity, ΔE_0, is equal to 368 cm^{-1} and ΔE_{90} is equal to 163 cm^{-1}, for a difference of about 200 cm^{-1}, where again the barrier to planarity is larger than the barrier to

perpendicularity. These may seem low, but 0° and 90° are representing energy wells, rather than barriers here, indicating that rather than having a barrier to be planar or perpendicular, there is a barrier to interconvert between the two. The barrier located at approximately -43° is about 863 cm^{-1} and the barrier at 47° is 1,404 cm^{-1}. Unlike the ground state potential energy surface, the lower energy configurations in the excited state are associated with more twisted or more planar conformations rather than a semi-twisted (close to 45°) conformation. The global minimum geometry is the bent structure shown in Figure 7, which has not been previously reported in the literature.
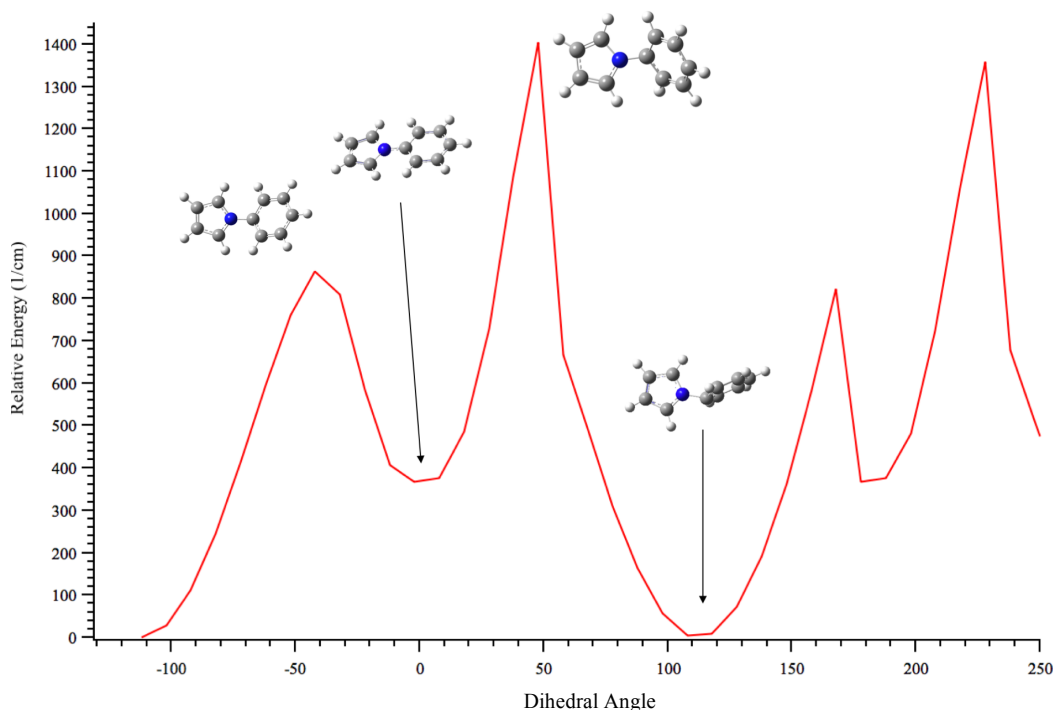
Figure 9: The 1PhPy bare chromophore excited state potential energy surface. The structure is shown at 0° and 113° (this corresponds to the 67.9° presented in Table 2, which was converted to a frame of reference between 0-90°), as well as the two transition states, -42° and 47°.

The ground state 1PhPy + 1H$_2$O potential energy scan is presented in Figure 10, showing different transition state energies to 1PhPy in the ground state. In particular, $\Delta E_0 = 1,033$ cm[-1], whereas ΔE_{90} is significantly reduced to 174 cm^{-1}. For 1PhPy + 1H$_2$O, ΔE_0 is much larger than

ΔE_{90} by about 800 cm^{-1} as opposed to only 70 cm^{-1} for 1PhPy . As observed in the figure, the water molecule prefers to interact with the pyrrole ring through a hydrogen atom-π stabilization.
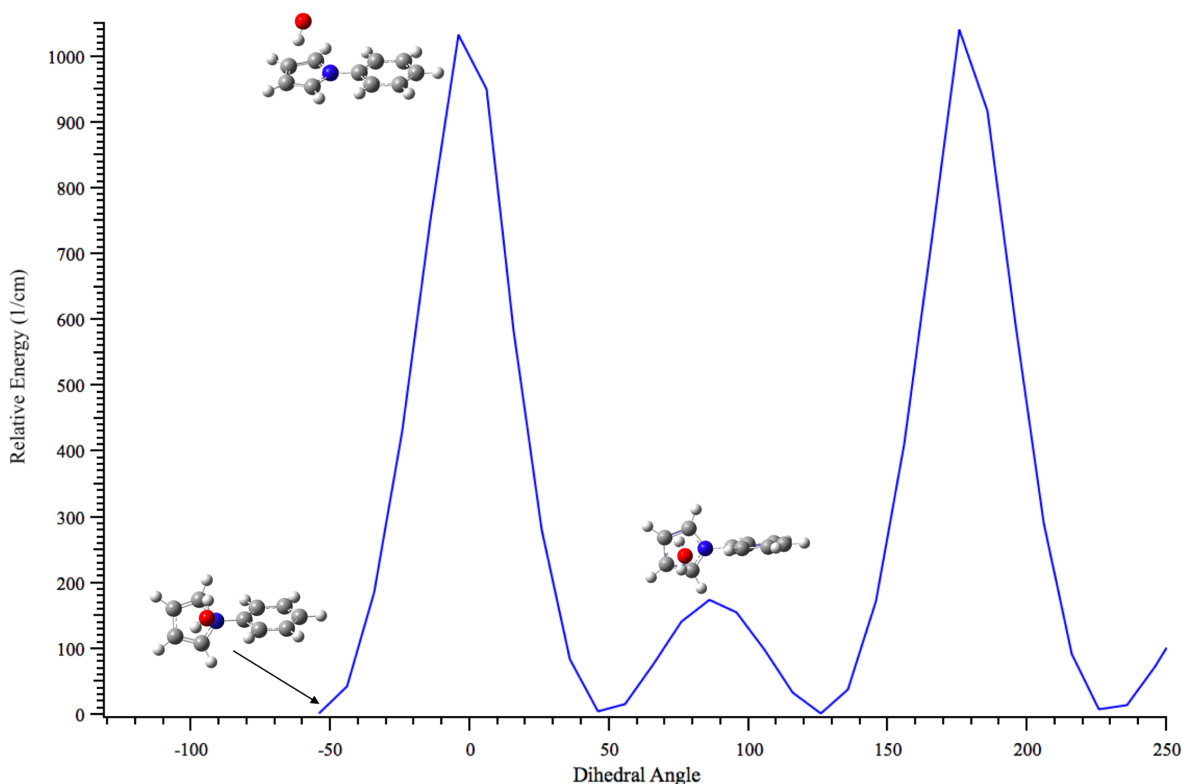
Figure 10: The ground state potential energy surface for 1PhPy + 1H$_2$O. The structure is shown at -50˚ (the minimum energy conformation), 0˚ (ΔE_0), and 90˚ (ΔE_{90}), respectively.

As shown in Figure 11, the potential energy surface pattern for 1PhPy + 1H$_2$O in the excited state changes drastically. Here, $\Delta E_0 = 2,371$ cm^{-1}, which is twice the energy than in the ground state. Strikingly, there is no longer a barrier to perpendicularity. Furthermore, the global minimum on the excited state resembles the geometry of the 1PhPy bare chromophore such that the pyrrole ring is bent towards the phenyl ring, with the water molecule bridging the two π systems as both a hydrogen atom donor and acceptor.
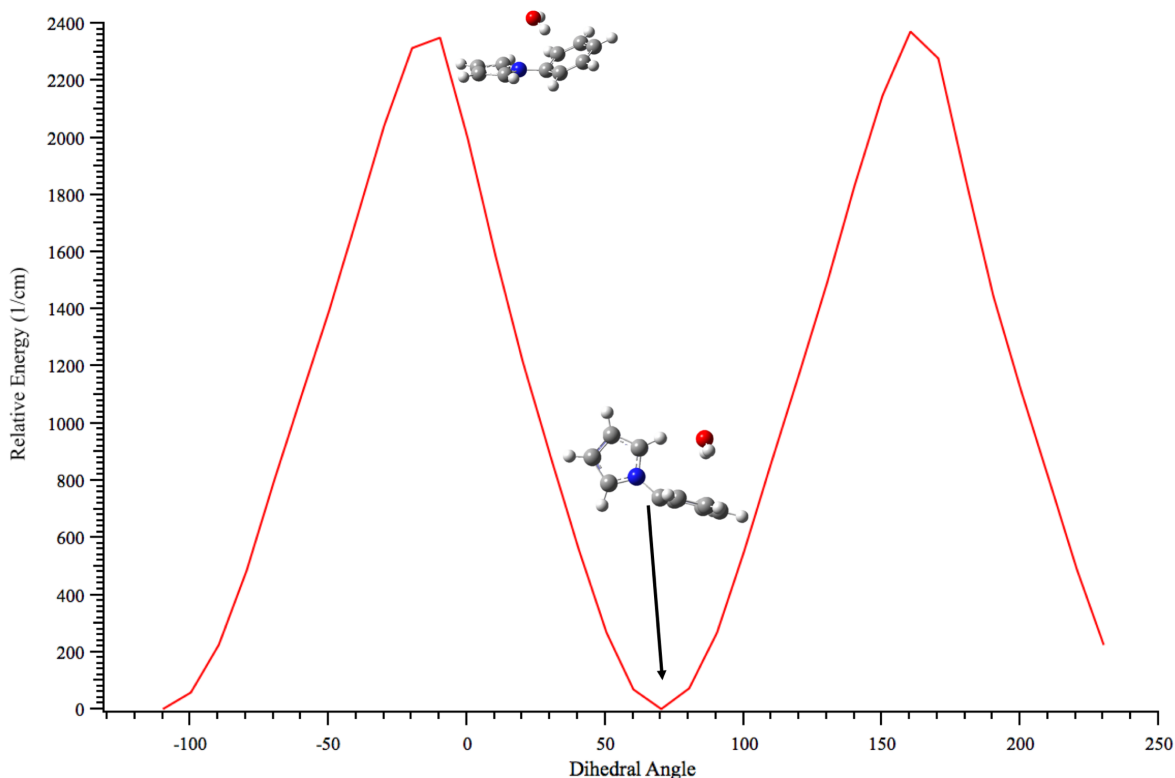
Figure 11: The excited state potential energy surface for 1PhPy + 1H$_2$O. The structure is shown at approximately 0° (ΔE_0), and the energy minimum at approximately 70°.

For the 1PhPy + 2H$_2$O ground state potential energy scan presented in Figure 12, there are two ΔE_{90}. From left to right across the transition state energies with structures next to them, the first transition state barrier is the first barrier to perpendicularity (ΔE_{90}=643 cm^{-1}). The second transition state barrier is ΔE_0, which is equal to 887 cm^{-1}. The third transition state barrier is the second ΔE_{90}, which is equal to 1,818 cm^{-1}. At 140°, there is a local minimum in a semi twisted configuration. The first ΔE_{90} is smaller than ΔE_0 by about 250 cm^{-1}, while the second ΔE_{90} is larger by ΔE_0 by about 930 cm^{-1}. From examining the transition state geometries, the position of the water molecule changes across the dihedral angle scan. At the ΔE_{90} with a lower value, the two water molecules are positioned more directly over the pyrrole ring, whereas at the higher-energy ΔE_{90}, the water molecules interact with the phenyl ring. The difference between the local and global minima is also due to solvent position, where at 140° the water is located above the phenyl ring

and at 220° the water is interacting with the pyrrole ring. The importance of water solvent in facilitating charge transfer and changing the barriers to twisting will be more fully explored in the Discussion section.

Figure 12: The ground state potential energy surface for 1PhPy + 2H$_2$O. The structure is shown at approximately -90° (ΔE_{90}), 0° (ΔE_0), 90° (ΔE_{90}), 140°, and the energy minimum, at about 220°.

From the 1PhPy + 2H$_2$O potential energy scan in the excited state (Figure 13), ΔE_0 is equal to 1,549 cm^{-1} and ΔE_{90} is equal to 791 cm^{-1}. The energy minimum has a dihedral angle of 114°, which is closer to a perpendicular rather than planar conformation. When adjusted to a value between 0-90°, this becomes the 74.1 values reported in Table 2. The barriers to twisting are not located at 0° or 90°, indicating that while the molecule may exist in a planar or perpendicular geometry in a local minimum, it may not easily be able to convert between the two. Again, the lowest-energy geometry is consistent with the bent geometry found for the 1PhPy bare chromophore and 1PhPy + H$_2$O.

Figure 13: The excited state potential energy surface for 1PhPy + 2H$_2$O. The structure is shown at approximately -90˚ (ΔE_{90}), 0˚ (ΔE_0), and the energy minimum, at about 114˚.

Similar to the 1PhPy + 2H$_2$O molecular complex, there are multiple barriers to perpendicularity and planarity found for the 1PhPy + 3H$_2$O ground state potential energy surface shown in Figure 14. The two ΔE_{90} are equal to 1,397 cm^{-1} and 900 cm^{-1}, corresponding to the first and fourth structures in Figure 14. The two ΔE_0 are equal to 1,887 cm^{-1} and 461 cm^{-1}, corresponding to the second and third structures in Figure 14. Upon closer inspection, the barriers to planarity and perpendicularity may be due to the migration of the water molecules as the dihedral angle changes. In particular, the higher-energy barriers are associated with the water molecules arranging themselves between the two aromatic rings or localized on the phenyl ring. However, the 1PhPy + 3H$_2$O geometries with lower-energy barriers reveal more localized interaction with the pyrrole unit of 1PhPy. We will discuss this point in further detail as it relates to charge transfer in the Discussion section.
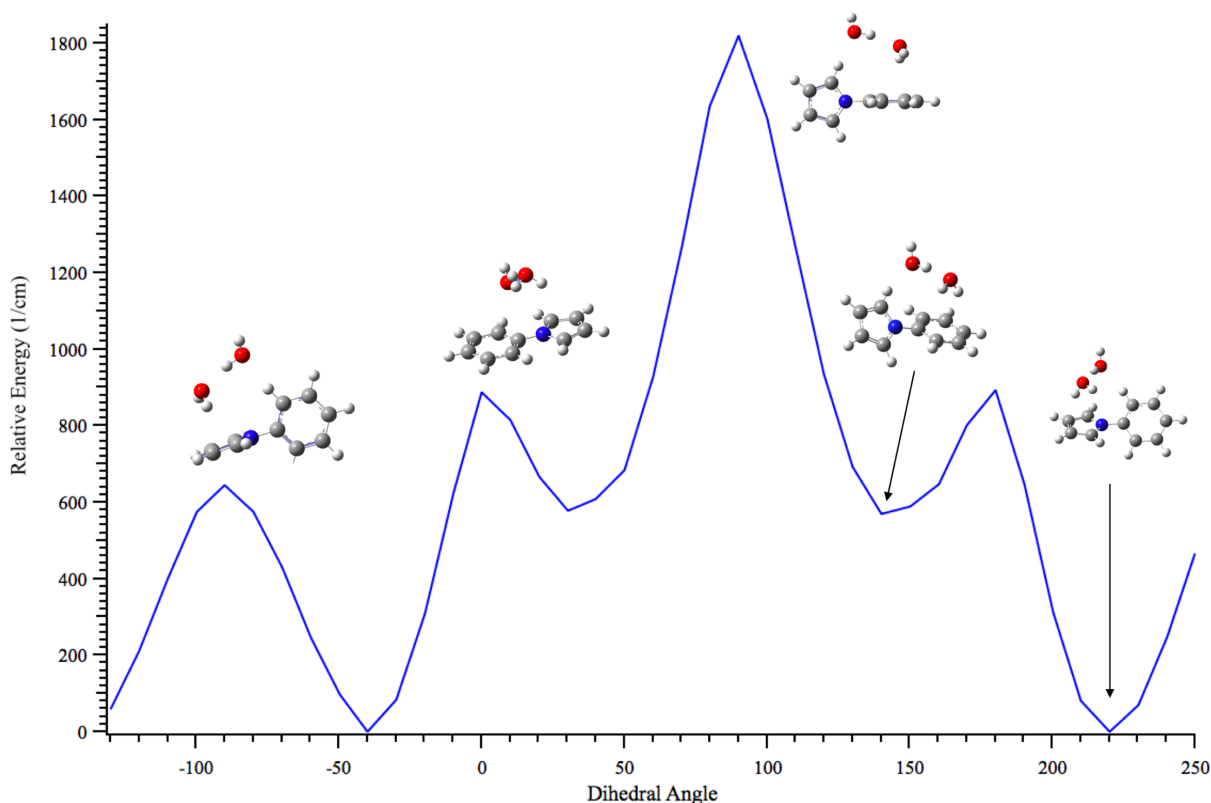
28
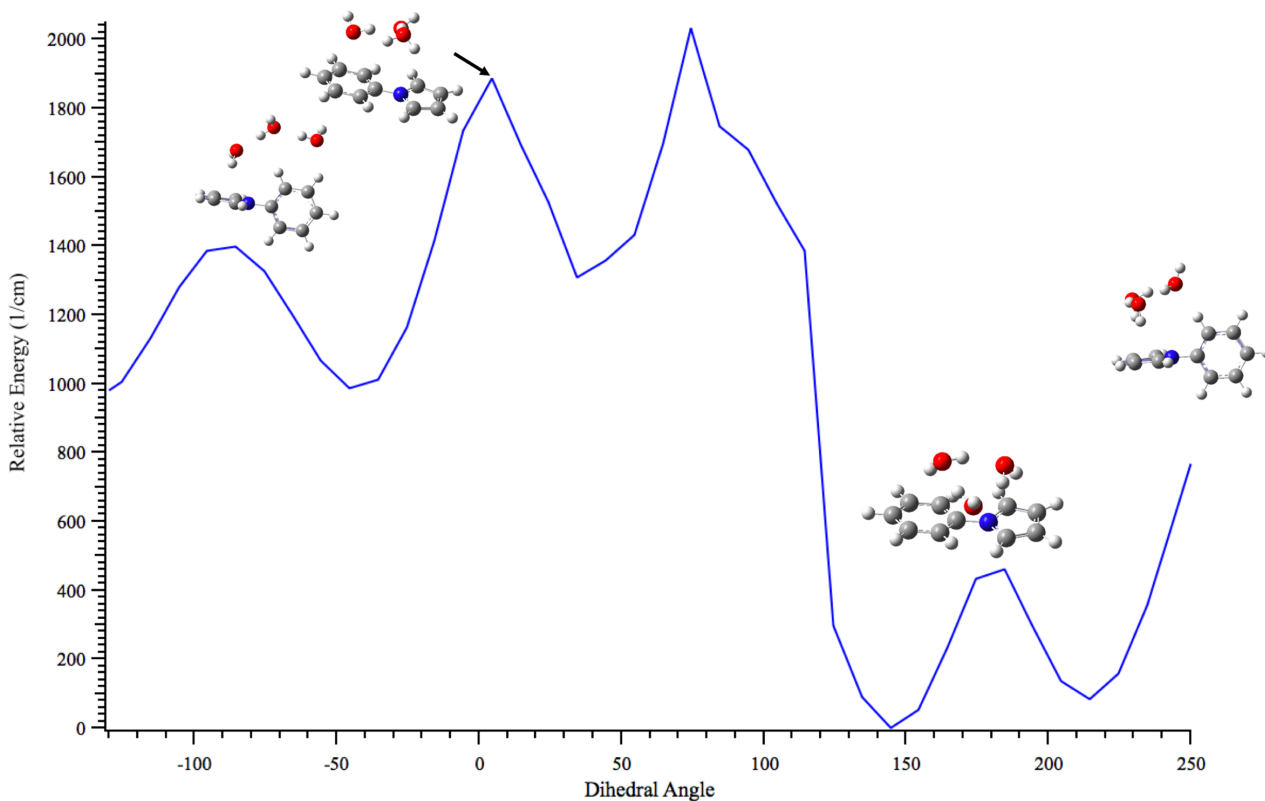
Figure 14: The ground state potential energy surface for 1PhPy + 3H$_2$O. The structure is shown at approximately -90° (ΔE_{90}), 0° (ΔE_0), 180° (ΔE_0), and 270° (ΔE_{90}).

The potential energy surface for the excited state of 1PhPy + 3H$_2$O in Figure 15 is unique in that the excited state barriers are lower in energy than the corresponding ground state barriers. Since the optimal structure for the excited state has a dihedral angle at 90°, motion to overcome perpendicularity is barrierless (ΔE_{90} = 0). Furthermore, ΔE_0 is approximately 1100 cm^{-1} for structures at both 0° and 180°.
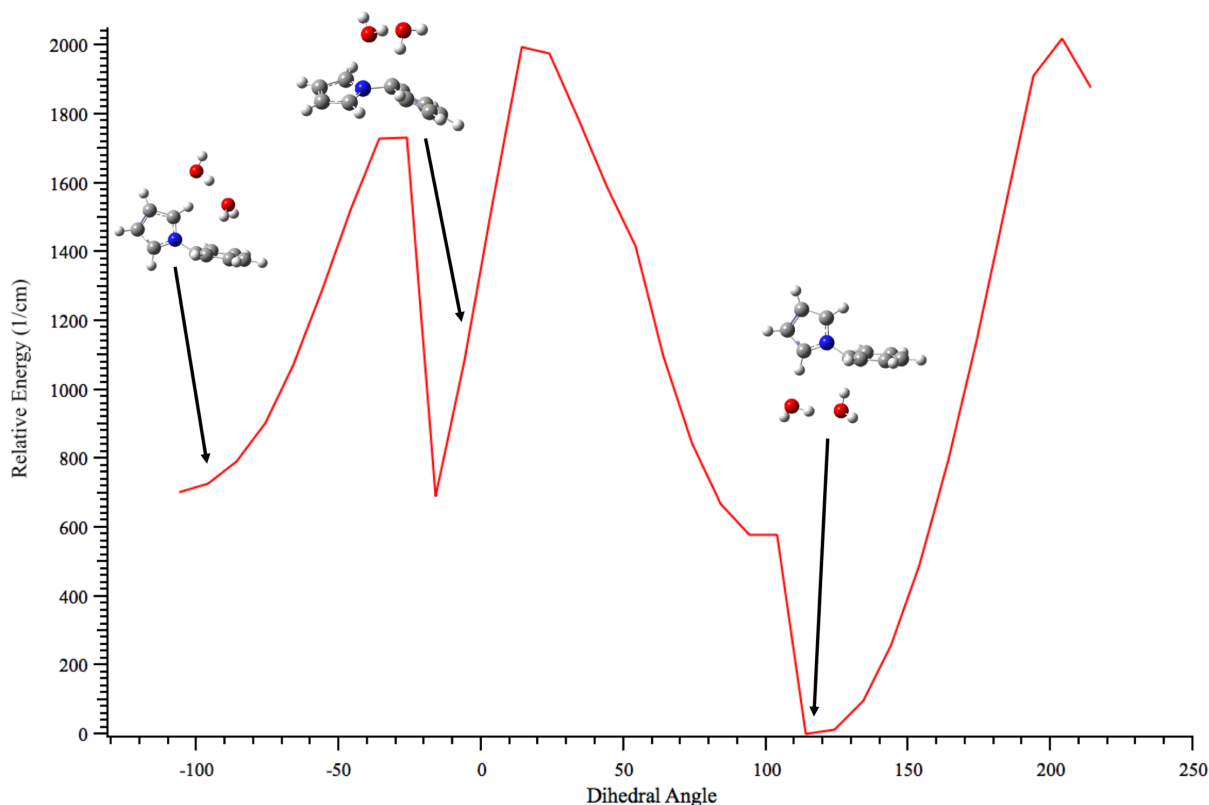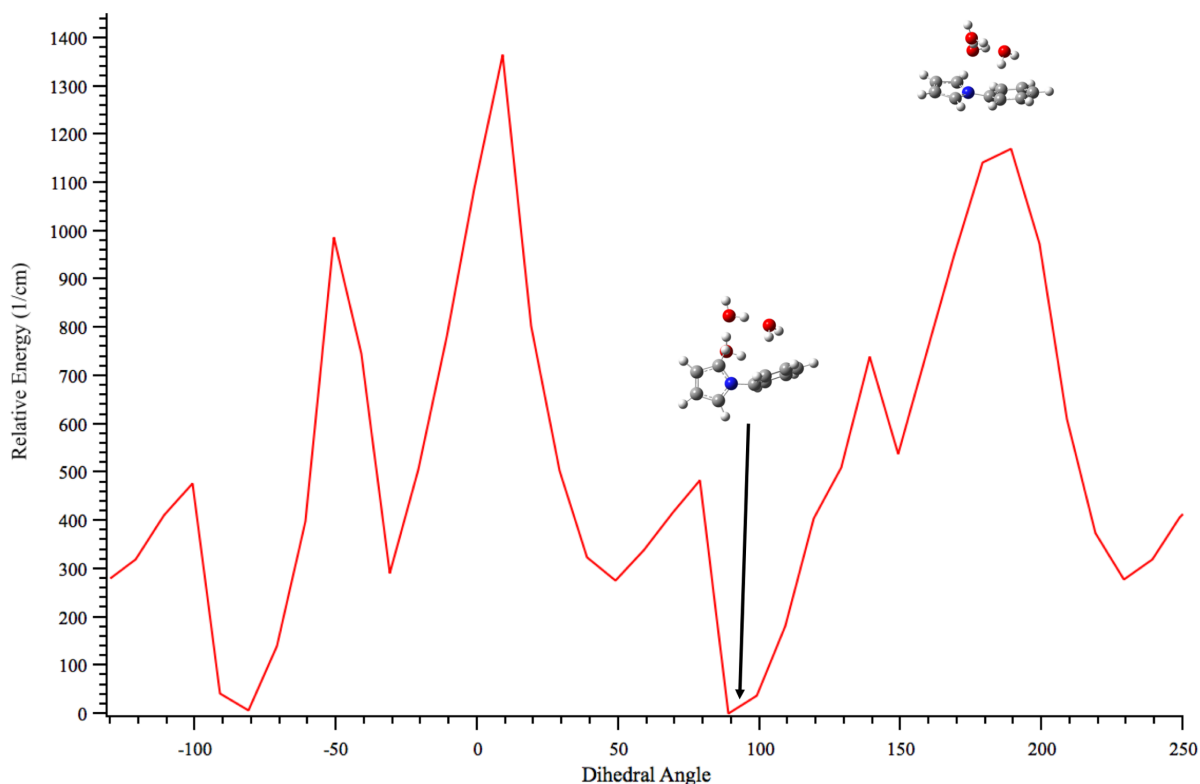
Figure 15: The excited state potential energy surface for 1PhPy + 3H$_2$O. The structure is shown at approximately 90˚ (ΔE_{90}) and 180˚ (ΔE_0). This was run with a 6-31G ++ (d,p) basis set rather than a 6-311G ++ (d,p) basis set due to computational costs.

A summary of all the barriers discussed in the potential energy surfaces is provided in Table 4.

Table 4: A summary of the barriers to planarity (ΔE_0) and perpendicularity (ΔE_{90}) for each complex in the ground and excited electronic states.

	Ground State		Excited State	
	ΔE_0 (cm^{-1})	ΔE_{90} (cm^{-1})	ΔE_0 (cm^{-1})	ΔE_{90} (cm^{-1})
1PhPy	652	579	368	163
1PhPy + 1H$_2$O	1,033	174	2,371	0
1PhPy + 2H$_2$O	887	643; 1,818	1,549	791
1PhPy + 3H$_2$O	1,887; 461	1,397; 900	1,100	0

3.2 Comparison of Theoretical Prediction and Experimental Results

We now turn to a comparison between the theoretical calculations in Tables 2 and 3 with the experimental UV/Vis spectra taken for 1PhPy in water and acetonitrile shown in Figure 16. Typically, UV/Vis spectra recorded in acetonitrile better indicate the onset of the gas-phase R2PI spectrum more so than the analogous spectra taken in water. Comparing the two UV/Vis spectra, water as a solvent creates a blue-shift of the absorption maximum towards higher energy. However, the theoretical calculations in Tables 2 and 3 predict that electronic absorption occurs at lower energy for sequential addition of water ($1PhPy + nH_2O$) compared to the 1PhPy bare chromophore. This deviation may be due to the larger number of water molecules interacting with 1PhPy within the first solvation shell. Nevertheless, the results presented herein reveal the photophysical effects of 1PhPy following step-wise addition of water in order to provide a 'bottom-up' picture of aerosol environments.
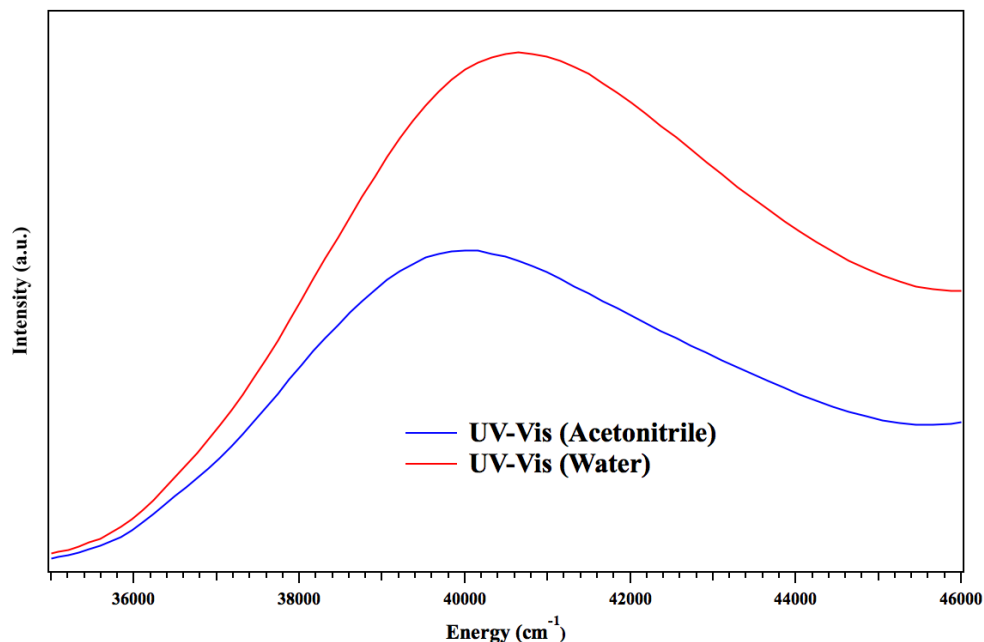
Figure 16: The UV-Vis spectra of 1PhPy taken on a Perkin Elmer lambda 35 UV/Vis spectrophotometer in two solvents. The blue line shows the spectra taken using acetonitrile as the solvent. The red line shows the spectrum using water as the solvent. Energy given in wavenumbers is on the x-axis with relative intensity on the y-axis.

3.3 Experimental Results

3.3.1 Bare chromophore

The R2PI spectrum for the bare 1PhPy molecule is superimposed on the UV/Vis spectra in Figure 17. The electronic origin band is at 35,490 cm^{-1}, which is due to a $v' = 0 \leftarrow v'' = 0$ transition from the ground to the excited electronic state. The vibronic transitions in the R2PI spectrum are found near the onset of absorption in the UV/Vis spectrum of 1PhPy recorded in acetonitrile solvent. Furthermore, a closer view of the R2PI spectrum is shown in the bottom panel of Figure 17, where there is a regular ~50 cm^{-1} spacing between vibronic transitions, in addition to further vibronic activity at higher energy. We attribute the transition peaks with ~50 cm^{-1} spacing to the torsion vibrational mode between the pyrrole and phenyl rings.
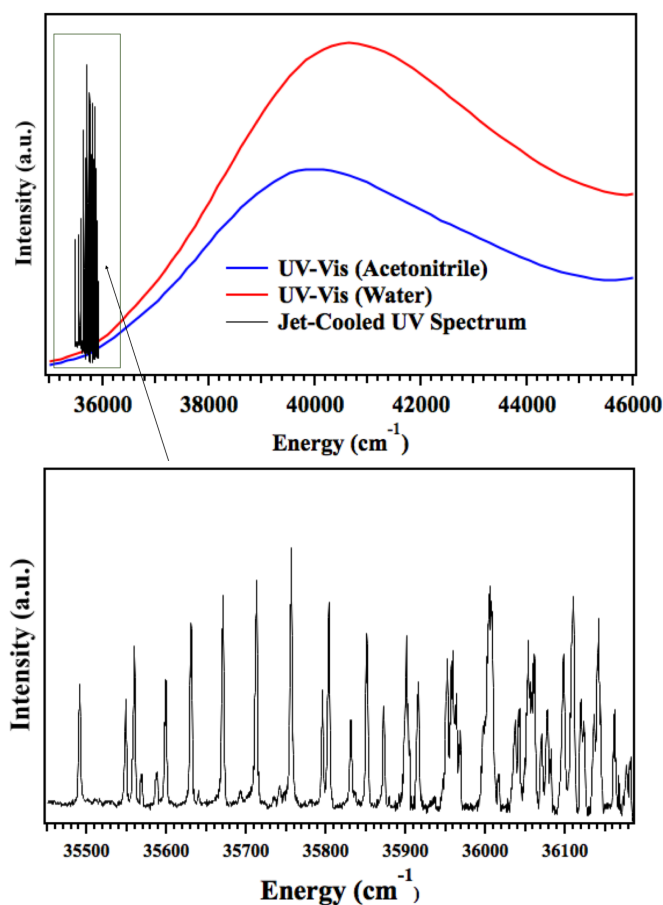
Figure 17: The UV/Vis spectrum of 1PhPy with the gas phase R2PI spectrum (top) and a blow up of the R2PI spectrum (bottom). The origin band is the peak located at 35490 cm^{-1}.

3.3.2 1PhPy + 1H₂O

Although ion signal was observed in the 1PhPy + $1H_2O$ mass channel, no resonant transitions were observed when the probe wavelength was scanned. However, when water was entrained in the supersonic jet expansion, new transition bands were found in the R2PI spectrum (Figure 18) at longer wavelengths when monitoring the 1PhPy mass ion signal. We assign these new features as arising from the 1PhPy + $1H_2O$ molecular complex decomposing to $1PhPy^+$ and water fragments following photoionization. The low-energy interaction between 1PhPy and water is likely exceeded upon ionization of the molecular complex. Similar to the bare 1PhPy chromophore, we observe regular spacing between the new vibronic transitions of approximately 70 cm⁻¹, which we assign to increasing quanta placed in the torsional mode. The bands labeled with asterisks are due to the bare 1PhPy chromophore transitions observed in the R2PI spectrum shown in Figure 17. Assignment of peaks and further analysis for both 1PhPy and the 1PhPy + $1H_2O$ complex will be presented in the Discussion section.

Figure 18: The R2PI spectrum recorded while monitoring 1PhPy (m/z=143) with water entrained in the supersonic expansion. The new vibronic features labeled with tie lines are attributed to 1PhPy + $1H_2O$. Peaks due to the bare chromophore are marked with asterisks.

Chapter 4: Discussion

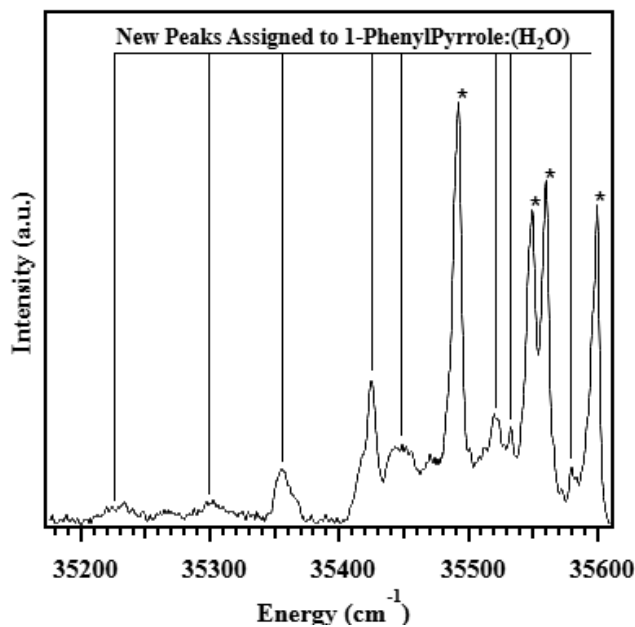Transition peaks were tentatively assigned in the R2PI spectra of 1PhPy (Figure 19) and 1PhPy + 1H$_2$O (Figure 22). The electronic origin band in the R2PI spectrum of 1PhPy is at approximately 35,490 cm^{-1}, which is similar to that reported by Okuyama et al. (1998) and Thomas et al. (2010). Okuyama et al. originally assigned alternating excited state vibronic bands with even quanta due to torsional transitions from v''=0 to v'=0, 2, 4, etc. (e.g., T_0^n), while also assigning odd number quanta to torsional transitions with v''=1 to v'=1, 3, 5, etc. (e.g., T_1^n). More recently, the high-resolution spectroscopy measurements recorded by Thomas et al. provided evidence that the torsional transitions originated from v''=0 since the rotational constants remained the same for each transition. Indeed, clear changes to the rotational constants would be evident in the rotationally-resolved spectra if the initial vibrational level were different than v''=0. As shown in Figure 8, the torsional barriers for 1PhPy are sufficiently large that the low-lying torsional energy levels will occur in degenerate pairs. For example, the T_{0+} and T_{0-} levels are degenerate but have vibrational wave functions that are symmetric and antisymmetric, respectively, with regard to the planar configuration. The selection rules governing the observed vibronic transitions dictates that the vibrational wave function has the same symmetry with respect to torsion in both the ground and excited electronic states. Therefore, the label $T_{0+/-}^n$ indicates the series of transitions T_{0+}^0, T_{0-}^1, T_{0+}^2, T_{0-}^3, etc.

We reassign the peaks with a ~50 cm^{-1} spacing between adjacent bands to both even and odd quanta in the torsional mode ($T_{0+/-}^n$) as originating from v''=0. The torsional modes labeled blue in Figure 19 represent motion along the dihedral angle of interest, i.e. rotation about the C-C bond between the phenyl and pyrrole rings. The geometry change between the ground and excited electronic states is calculated to be large, in which the excited state geometry adopts a bent

structure with the pyrrole ring oriented towards the phenyl group, giving rise to a long Franck-Condon progression and vibronic intensity profile.
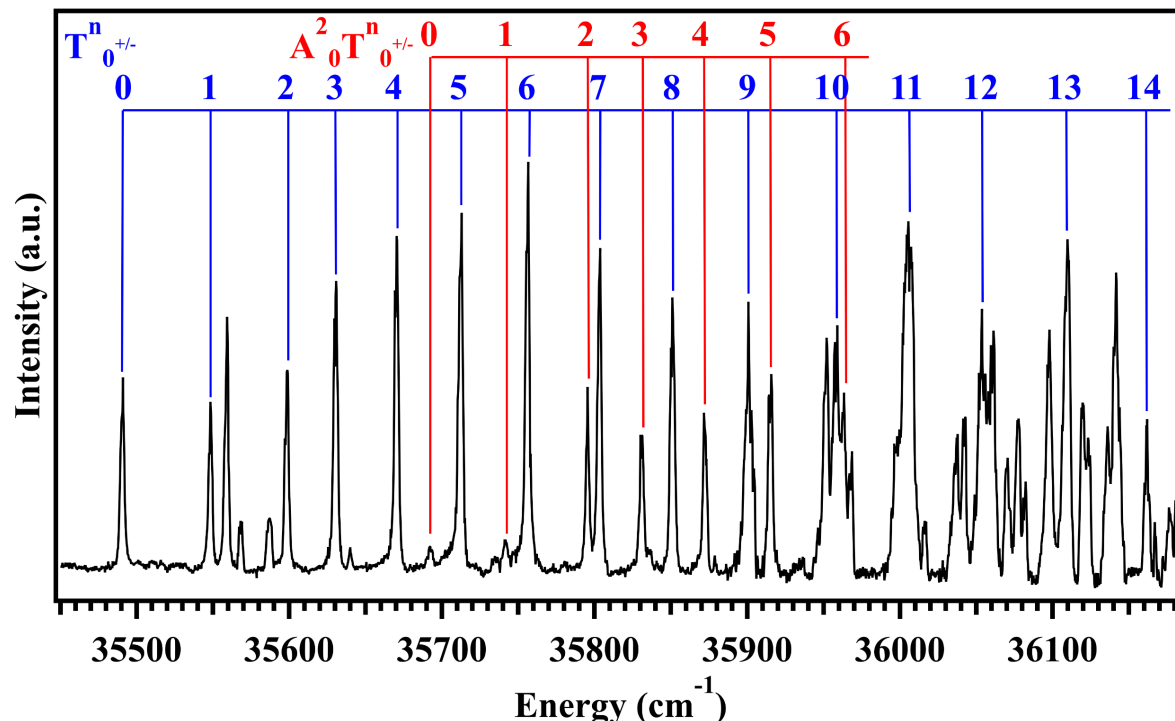
Figure 19: The R2PI spectrum of 1PhPy with peaks tentatively assigned. The $T^n_{0+/-}$ band is the torsional mode progression. The $A^2_0 T^n_{0+/-}$ band progression is a mixture of the torsional mode and another molecular motion. Vibronic bands are approximately 50 cm^{-1} apart.

The second series of progressions labeled in red is mentioned in the work by Okuyama et al., but the authors did not make an assignment of the possible vibrational modes. We ascribe this progression (labeled $A^2_0 T^n_{0+/-}$) to a combination band involving the torsional mode, $T^n_{0+/-}$, with another type of molecular motion since the spacing between vibronic peaks is approximately 50 cm^{-1}. In comparing the vibrational frequencies from our theoretical calculations to the energy difference between the electronic origin band and the beginning of the $A^2_0 T^n_{0+/-}$ progression (~200 cm^{-1}), the *A* mode may belong to a twisting motion between the two different rings (Figure 20) with a calculated frequency of 101 cm^{-1}. The overall symmetry of the vibronic wave functions

must be totally symmetric to be observed in the R2PI spectrum, which is accomplished with an even number of quanta in the *A* vibrational mode. The observed transitions in the progression would then be $A_0^2 T_{0+}^0$, $A_0^2 T_{0-}^1$, $A_0^2 T_{0+}^2$, $A_0^2 T_{0-}^3$, etc.
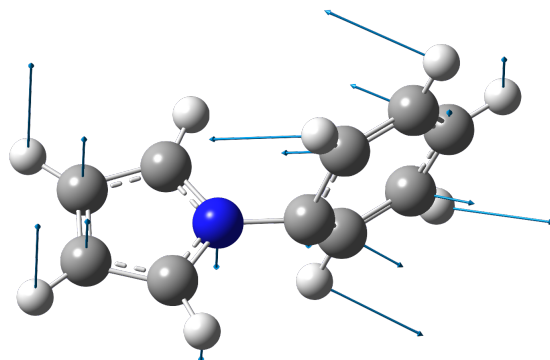
Figure 20: 1PhPy with arrows displaying the twisting–like vibrational mode.

As previously mentioned, there is a significant change in geometry between the ground and excited electronic states, in which the pyrrole ring is oriented towards the phenyl ring. Therefore, vibrational modes reflecting this geometry change may plausibly be activated and observed in the electronic spectrum. Another possible assignment of the $A_0^2 T_{0+/-}^n$ progression may involve the torsional mode combined with a bending-like motion between the pyrrole and phenyl rings shown in Figure 21, with a predicted frequency at 80 cm^{-1}. With two quanta along this bending-like mode, the predicted vibronic band would be in close agreement with the observed beginning of the $A_0^2 T_{0+/-}^n$ progression. To obtain the correct overall symmetry, the progression would similarly be $A_0^2 T_{0+}^0$, $A_0^2 T_{0-}^1$, $A_0^2 T_{0+}^2$, $A_0^2 T_{0-}^3$, etc.
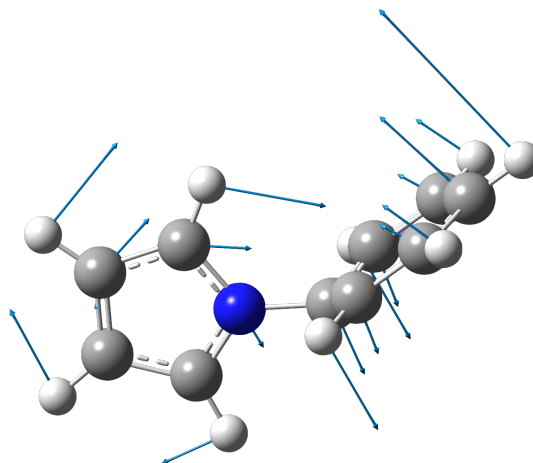
Figure 21: 1PhPy with arrows displaying the bending motion.

Turning to the R2PI spectrum for 1PhPy + $1H_2O$ shown in Figure 22, we assign the electronic origin band to the lowest energy peak observed at 35227 cm^{-1}, which is red-shifted from the 1PhPy bare chromophore origin by 263 cm^{-1}. The intermolecular interaction of water with 1PhPy can be best described as a weak Coulombic attraction (water binds as a proton donor to the aromatic ring) rather than a true hydrogen bond. The dihedral angle of 1PhPy with and without water complexation is 67° and 70°, respectively. Thus, the relative stabilization of this interaction is reflected in the modest red-shift of the 1PhPy + $1H_2O$ electronic origin band with respect to 1PhPy. Additionally, the weak interaction between 1PhPy and water may also explain the likely fragmentation of the 1PhPy + $1H_2O$ complex upon ionization, arising as new resonant features observed in the $1PhPy^+$ mass channel.

As shown in the figure, the vibronic peaks have been assigned in a similar fashion as the R2PI spectrum for 1PhPy. The transitions labeled blue in the figure have a spacing of approximately 70 cm^{-1}, which we assign to the torsional mode, $T_{0+/-}^n$ having a calculated vibrational frequency of 74 cm^{-1} in the excited state. Shown in Figure 11, the barrier to planarity

in the 1PhPy + 1H$_2$O excited state potential energy surface is larger by a factor of two compared to the bare chromophore excited state (Figure 9). We attribute the heightened barrier to the increase in the torsional mode vibrational frequency and therefore the observed peak spacing in the 1PhPy + 1H$_2$O R2PI spectrum.

Analogous to the 1PhPy R2PI spectrum, we assign the band at ~222 cm^{-1} above the electronic origin to the onset of the $A_0^2 T_{0+/-}^n$ progression. Here, the torsional and twisting or bending nuclear motions are also coupled; the nuclear motions of the twisting and bending modes of 1PhPy + 1H$_2$O are similar to the modes illustrated in Figures 20 and 21. For the 1PhPy + 1H$_2$O complex, the predicted frequency associated with the twisting motion is 114 cm^{-1}, which with two quanta would be in close agreement with the progression starting at 222 cm^{-1}. Furthermore, the bending mode has a calculated vibrational frequency of 93 cm^{-1}, which would be predicted to lie close to the observed vibronic band. Symmetry concerns must also be considered. 1PhPy has a clear plane of symmetry through the molecule with or without water complexation in the excited state, and therefore the same vibronic symmetry rules are expected to be similar to those described earlier for the 1PhPy bare chromophore. For future work, the torsional motion of 1PhPy and 1PhPy + 1H$_2$O will be simulated using an internal rotation model with two-fold periodicity. Our goal will be to obtain the predicted torsional energy levels and Franck-Condon factors to model the vibronic intensity distributions. Preliminary work along this regard using the potential energy surfaces shown in Figures 8-11 has shown promising results with the assignments made here.
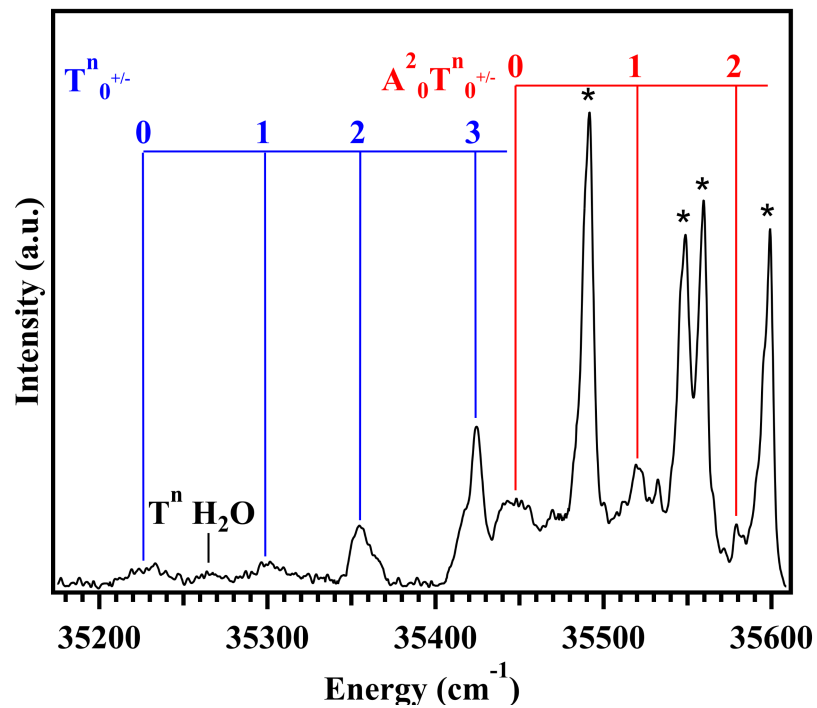
Figure 22: The R2PI spectrum of 1PhPy + 1H_2O with the torsional modes $T_{0+/-}^n$ assigned in blue and the $A_0^2 T_{0+/-}^n$ combination band in red. The peaks associated with the bare chromophore are marked with an asterisk.
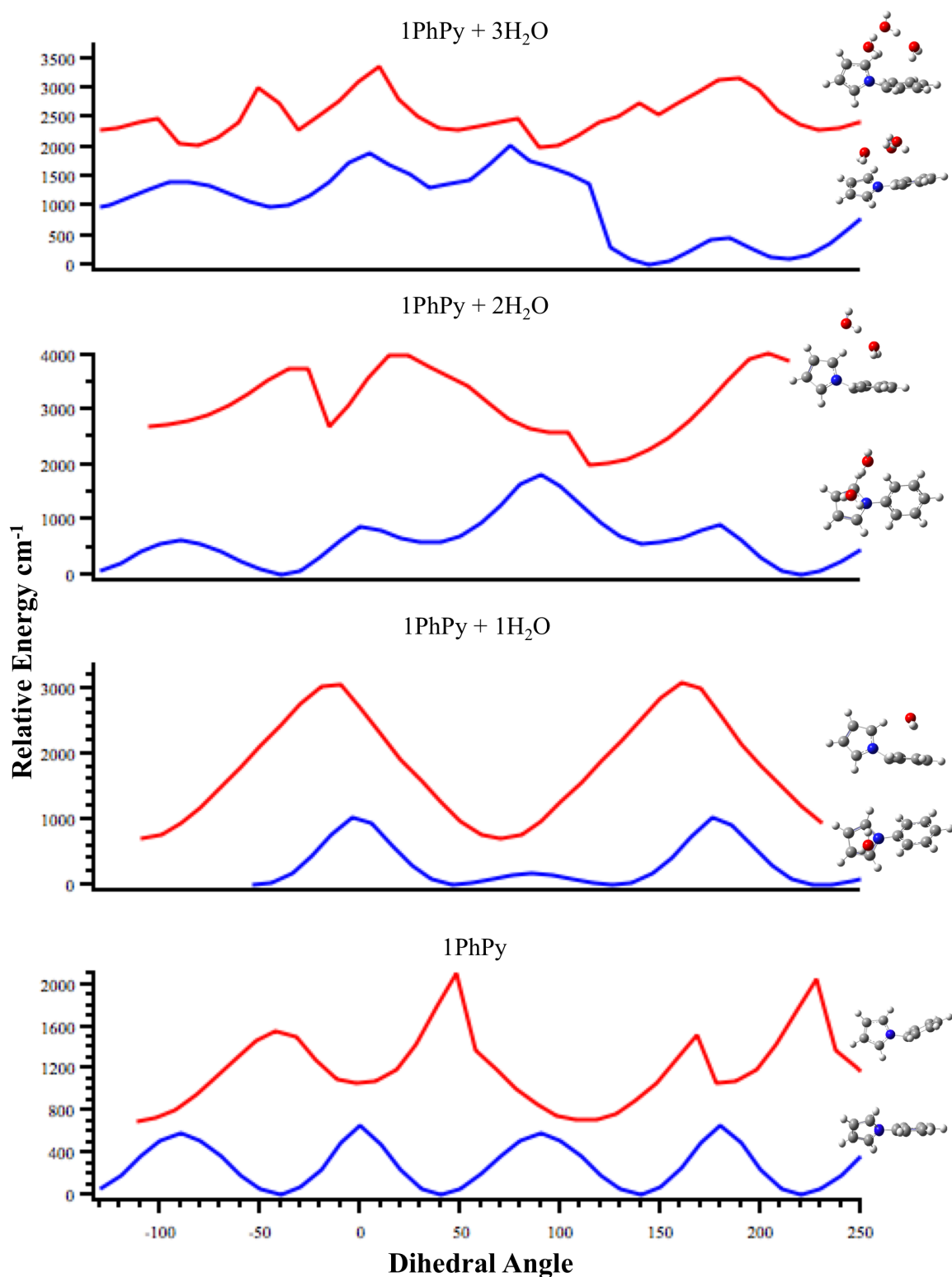
Figure 23: A summary of the ground and excited state potential energy scans for 1PhPy, 1PhPy+1H$_2$O, 1PhPy+2H$_2$O, and 1PhPy+3H$_2$O. The ground state is shown in blue and the excited-state is offset in red. The optimized geometry of each state is presented next to each line.

Shifting to the calculated potential surfaces shown in Figure 23, the ground state dihedral angle of 1PhPy (lower panel; blue trace) is predicted to be 40.2˚, which is comparable to the experimental result of 38.7˚ reported by Okuyama et al. (1998). In the ground state, 1PhPy is most stable in a semi-twisted conformation, and the barriers to perpendicularity (ΔE_{90}; dihedral angle=90°) and planarity (ΔE_0; dihedral angle=0°) in the ground state are 579 cm^{-1} and 652 cm^{-1}, respectively. For the excited state potential energy scan for 1PhPy shown as the red trace in the lower panel, the initial dihedral angle was found to be 113˚ or 67.9˚, when put in a frame of reference between 0-90˚, which contrasts the 19.8˚ dihedral angle for the optimal configuration determined by Okuyama. However, the optimal geometry determined by Okuyama is close to the local minimum geometry found in the excited state potential energy scan for 1PhPy (red trace). The first optimization calculation completed for this experiment did generate this more planar geometry similar to Okuyama. However, the potential energy scan results point to an optimal excited state geometry with a dihedral angle of 113˚, which did not have any negative frequencies that are indicative of a transition state. The lowest-energy conformer adopts a bent structure, wherein the C-H pyrrole bond stabilizes the π* orbital on the phenyl ring upon excitation. Therefore, the excited state of 1PhPy adopts a geometry that more readily facilitates twisted intramolecular charge transfer (TICT).

Visualizing the movement of charge that occurs when the molecule is excited is also useful for understanding the TICT of 1PhPy. To this end, calculations were carried using Gaussian out to obtain electron density difference maps for several dihedral angles of interest for 1PhPy illustrated in Figure 24. Cyan shows the areas of electron depletion within 1PhPy, while purple shows the areas of electron density gain upon excitation from the ground to excited electronic state. Charge transfer appears to occur from the pyrrole group to the phenyl group in most conformations of the

molecule, except when the dihedral angle is at an energetic maximum or approaches planarity. As illustrated in the figure, 1PhPy shows minimal charge transfer at the transition state geometry (47˚) and at planar dihedral angles (0˚ or 180˚). However, charge transfer from the pyrrole ring donor to the phenyl ring acceptor is significant when 1PhPy adopts the lowest-energy bent configuration with a dihedral angle of 113°. Other dihedral angles demonstrate charge transfer to varying extents.

| 0˚ | 47˚ | 113˚ |

Figure 24: Electron difference density maps revealing the charge transfer across 1PhPy at different conformations. Cyan indicates the initial electron density in the HOMO and purple represents the final density shift to the LUMO after excitation.

Since solvent interactions are predicted to increase the likelihood of TICT in the previous literature, we expect different photophysical behavior for 1PhPy when it complexed with water (Proppe et al., 2000; Sasaki et al., 2016). As seen in Figure 23, the ground state barrier to perpendicularity is much lower for 1PhPy + $1H_2O$ than the 1PhPy bare chromophore. The energetic difference is even more striking as revealed in the 1PhPy + $1H_2O$ excited state potential energy scan results. With the addition of a single water molecule, there is no barrier to perpendicularity. In fact, the nearly perpendicular conformation is the lowest-energy configuration with barriers located at planarity (0˚ and 180˚). The agreement between the R2PI spectrum and the preliminary Franck-Condon torsional mode simulations for 1PhPy + $1H_2O$ further indicates a substantial decrease in energy for ΔE_{90}, further supporting that TICT is enhanced with water solvation. Close inspection of the 1PhPy + $1H_2O$ electron density difference maps in Figure 25

shows that charge transfer is evident at all the conformations, particularly when the 1PhPy chromophore in the complex resembles the bent geometry. These results indicate that water solvent interactions are extremely important in facilitating TICT for 1PhPy. Furthermore, we note the water solvent response to electronic excitation of 1PhPy. The water solvent acts as a reporter of charge transfer, wherein it migrates from the pyrrole ring in the ground state to a localized interaction with the phenyl ring in the excited state.
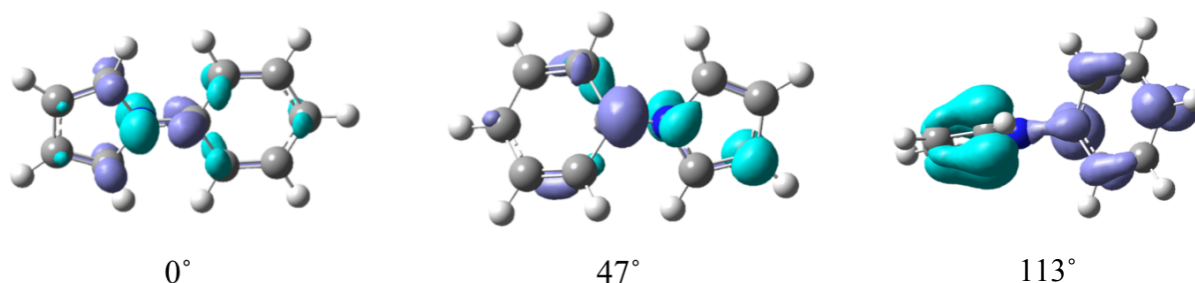

0°   **70°**

Figure 25: Electron difference density maps revealing the charge transfer across 1PhPy + 1H$_2$O at different conformations. Cyan indicates the initial electron density in the HOMO and purple represents the final density shift to the LUMO after excitation.

To further explore the importance of water solvation in facilitating TICT in 1PhPy, we carried out analogous calculations for 1PhPy + nH$_2$O (n=2, 3). Figure 26 shows that charge transfer occurs for 1PhPy + 2H$_2$O at all dihedral angles, even for planar and perpendicular geometries. This is reflected in the potential energy surface as well, where a more twisted geometry is the lowest energy conformation of the excited state for 1PhPy + 2H$_2$O (Figure 23). 1PhPy + 3H$_2$O continues this trend. Similar to the bare chromophore, the excited state structure optimized to two structures. The first optimized structure exhibits a dihedral angle fairly close to planar. The potential energy surface scan results indicate that the geometry with a dihedral angle of 90° is the energetic minimum (Figure 23). When the optimization calculation was completed again by setting the angle to about 90°, the 90° conformer was the lowest energy structure by about 2000 cm^{-1}. As also

observed for the 1PhPy bare chromophore, this energy difference with dihedral angle may be due to the fact that the 0˚ conformer is in a fairly straight position between rings, but the 90˚ conformer adopts the bent structure. For both 0˚ and 180˚ conformations, charge transfer is enabled (Figure 27).
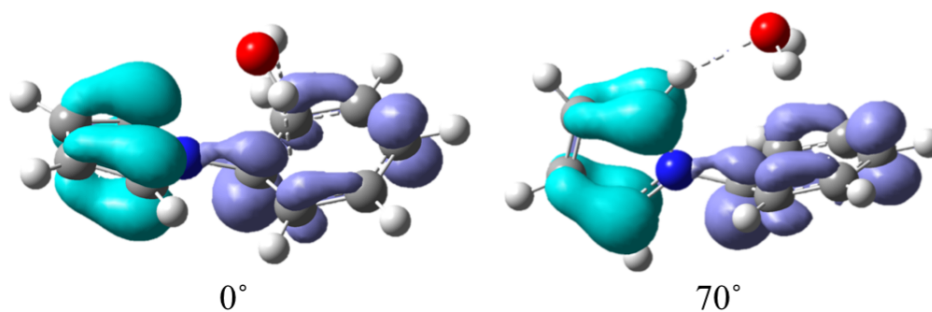

<div align="center">74.1˚   0˚</div>

Figure 26: Electron difference density maps revealing the charge transfer across 1PhPy + 2H$_2$O at different conformations. Cyan indicates the initial electron density in the HOMO and purple represents the final density shift to the LUMO after excitation.
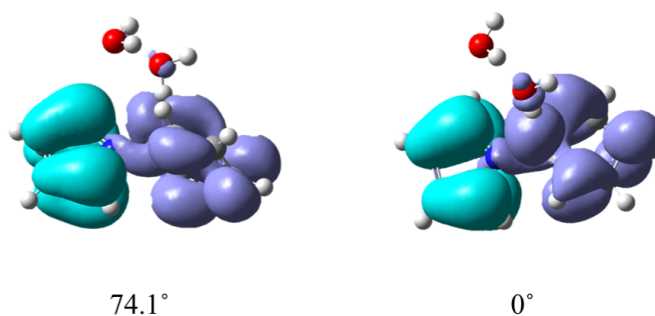

<div align="center">0˚   90˚</div>

Figure 27: Electron difference density maps revealing the charge transfer across 1PhPy + 3H$_2$O at different conformations. Cyan indicates the initial electron density in the HOMO and purple represents the final density shift to the LUMO after excitation.
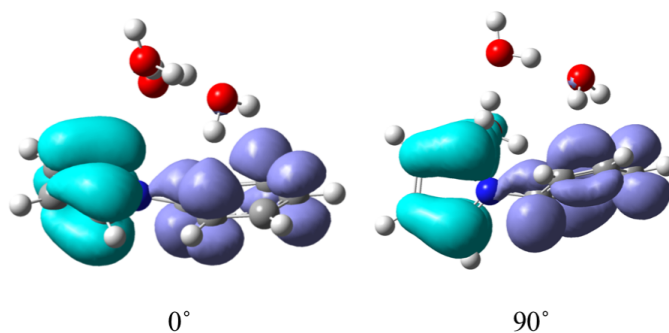
Chapter 5: Conclusions

From the results presented in this paper, 1PhPy can maintain its TICT molecule status. The large barriers to perpendicularity as described in previous literature (Okuyama et al., 1998; Proppe et al., 2000; Thomas et al., 2010) were not present when comparing our theoretical and experimental results. Additionally, unlike previous studies, the lowest energy conformation of 1PhPy became more perpendicular after excitation, adopting a bent structure to facilitate the pyrrole stabilization with the phenyl ring.

These results were further supported by the R2PI data. Torsional transitions $T_{0+/-}^n$ for the bare 1PhPy spectrum were reassigned from those in previous studies. Similar assignments for the 1PhPy + 1H$_2$O spectrum were made and motion for the combination $A_0^2 T_{0+/-}^n$ band in both spectra was proposed with backing from computational data.

The effect of water solvent in facilitating the TICT process for 1PhPy is striking. The addition of one water molecule removed the excited state barrier to perpendicularity, while increasing the barrier to planarity, effectively locking 1PhPy in a twisted conformation (Figure 11). The electron density difference maps show this clearly as well when water molecules are involved. In particular, charge transfer is occurring across all conformations of the molecule, planar or perpendicular. When three water molecules are complexed with 1PhPy, the lowest-energy configuration becomes the perpendicular conformation. Therefore, water is important in acting as a bridge for charge transfer to occur.

Within the context of atmospheric implications, the water cluster studies mimic the immediate solvation shell interactions for 1PhPy found in aerosol environments. From our analysis, 1PhPy should be considered a TICT molecule, where its geometry facilitates absorbance to overlap more strongly with solar flux. Consequently, solar absorption may promote secondary atmospheric

reactions and contribute to radiative forcing as a BrC chromophore. Overall, through the combined use of computational and experimental tools, we were able to obtain a molecular-level understanding of 1PhPy under aerosol like conditions, to further understand atmospheric processes.

Chapter 6: Future Study

6.1 Other pyrrole derivatives as potential brown carbon chromophores

Pyrrole derivatives are relevant as reactants, intermediaries, and products in brown carbon atmospheric chemistry. Analyzing the properties of 1PhPy and its classification as a TICT molecule is simply the tip of the iceberg. It would be chemically ludicrous to not consider other pyrrole derivatives as such.

As part of the work completed for 1PhPy, eight other molecules were computationally analyzed as described in the methods, excluding the potential energy surface scans. Many of them had multiple low-energy conformers and are given the designation of 1, 2, etc. (Table S1). These molecules are bipyrrole, n-benzylpyrrole, 2-benzylpyrrole, 3-benzylpyrrole, 2-phenylpyrrole, 3-phenylpyrrole, and then two experimentally proposed structures designated as "Experimental 1" and "Experimental 2". These experimental structures were taken from Kampf et al., 2016) (Figure S1). Ground state calculations for 1, 2, and 3 water molecules were done of each of the molecules, as well as some excited state calculations for the water clusters. Analyzing each of these molecules the way 1PhPy was done throughout this study would be an excellent next step in further understanding pyrrole derivatives and their role in brown carbon chemistry.

6.2 Further experimental methods for studying 1PhPy

6.2.1 Hole burning Spectroscopy

In order to determine if the new vibronic features are due to the 1PhPy + 1H$_2$O complex, hole burning spectroscopy can also be used to identify different isomers or conformers in gas-phase molecules free from the interference of other species in the supersonic jet expansion. By using gas-phase molecules in cold jet conditions, detailed information about the relative contributions to the R2PI spectrum from multiple isomers and/or conformations (Ullrich et al.,

2000). Using a pump laser to saturate a vibronic transition in the R2PI spectrum, the isomer and/or conformation population responsible for that transition is depleted. Therefore, a probe laser measures the ion signal depletion as a function of wavelength to isolate the transitions due to a unique isomer and/or conformation. Therefore, hole-burning spectroscopy could be used to verify that the new transitions in the R2PI spectrum are due to $1PhPy + 1H_2O$ to confirm the results given by our computational calculations.

6.2.2 Velocity Map Imaging

Velocity map imaging is a way to analyze the kinetic energy and distribution of photofragments of a molecule, following its dissociation. In this setup, a pump laser breaks apart the molecule of interest, and then the probe laser is able to selectively ionize a target photofragment (Figure 28). This charged photofragment then travels down the chamber until it hits the detector which causes it to illuminate as the ions collide. A camera is then able to catch those luminescence patterns and those images can be analyzed for information about those photofragments. Future work will focus on photolyzing 1PhPy at shorter wavelengths to induce photochemical bond breaking mechanisms.
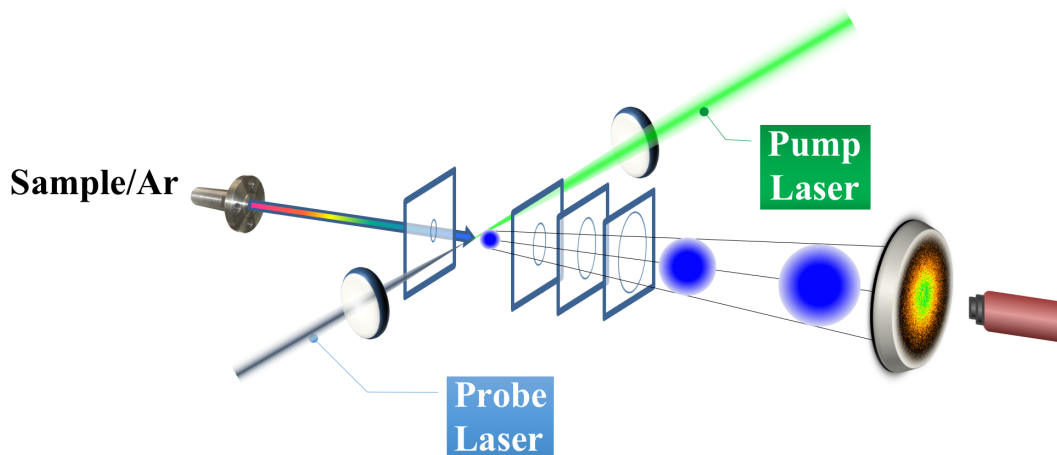

Figure 28: Overview of velocity map imaging.

Works Cited

(1) Lary, D. J., Lee, A. M., Toumi, R., Newchurch, M. J., Pirre, M., & Renard, J. B. (1997). Carbon aerosols and atmospheric photochemistry. *Journal of Geophysical Research: Atmospheres*, *102*(D3), 3671-3682.

(2) Chung, S. H., & Seinfeld, J. H. (2002). Global distribution and climate forcing of carbonaceous aerosols. *Journal of Geophysical Research: Atmospheres*, *107*(D19), AAC-14.

(3) Bergstrom, R. W., Russell, P. B., & Hignett, P. (2002). Wavelength dependence of the absorption of black carbon particles: Predictions and results from the TARFOX experiment and implications for the aerosol single scattering albedo. *Journal of the Atmospheric Sciences*, *59*(3), 567-577.

(4) Turpin, B. J., Saxena, P., & Andrews, E. (2000). Measuring and simulating particulate organics in the atmosphere: problems and prospects. *Atmospheric Environment*, *34*(18), 2983-3013.

(5) Andreae, M. O., & Gelencsér, A. (2006). Black carbon or brown carbon? The nature of light-absorbing carbonaceous aerosols.

(6) Liu, C., Chung, C. E., Yin, Y., & Schnaiter, M. (2018). The absorption Ångström exponent of black carbon: from numerical aspects. *Atmospheric Chemistry & Physics*, *18*(9).

(7) Desyaterik, Y., Sun, Y., Shen, X., Lee, T., Wang, X., Wang, T., & Collett, J. L. (2013). Speciation of "brown" carbon in cloud water impacted by agricultural biomass burning in eastern China. *Journal of Geophysical Research: Atmospheres*, *118*(13), 7389-7399.

(8) Bergstrom, R. W., Pilewskie, P., Russell, P. B., Redemann, J., Bond, T. C., Quinn, P. K., & Sierau, B. (2007). Spectral absorption properties of atmospheric aerosols.

(9) Laskin, A., Laskin, J., & Nizkorodov, S. A. (2015). Chemistry of atmospheric brown carbon. *Chemical reviews*, *115*(10), 4335-4382.

(10) Kirchstetter, T. W., Novakov, T., & Hobbs, P. V. (2004). Evidence that the spectral dependence of light absorption by aerosols is affected by organic carbon. *Journal of Geophysical Research: Atmospheres*, *109*(D21).

(11) Rizzo, L. V., Correia, A. L., Artaxo, P., Procópio, A. S., & Andreae, M. O. (2011). Spectral dependence of aerosol light absorption over the Amazon Basin. *Atmospheric chemistry and physics*, *11*(17), 8899.

(12) Sandradewi, J., Prévôt, A. S., Szidat, S., Perron, N., Alfarra, M. R., Lanz, V. A., ... & Baltensperger, U. R. S. (2008). Using aerosol light absorption measurements for the quantitative determination of wood burning and traffic emission contributions to particulate matter. *Environmental science & technology*, *42*(9), 3316-3323.

(13) Mukai, H., & Ambe, Y. (1986). Characterization of a humic acid-like brown substance in airborne particulate matter and tentative identification of its origin. *Atmospheric Environment (1967)*, *20*(5), 813-819.

(14) Dinar, E., Riziq, A. A., Spindler, C., Erlick, C., Kiss, G., & Rudich, Y. (2008). The complex refractive index of atmospheric and model humic-like substances (HULIS) retrieved by a cavity ring down aerosol spectrometer (CRD-AS). *Faraday discussions*, *137*, 279-295.

(15) Chen, Y., & Bond, T. C. (2010). Light absorption by organic carbon from wood combustion. *Atmospheric Chemistry & Physics*, *10*(4).

(16) Hand, J. L., Malm, W. C., Laskin, A., Day, D., Lee, T. B., Wang, C., ... & Iedema, M. J. (2005). Optical, physical, and chemical properties of tar balls observed during the Yosemite Aerosol Characterization Study. *Journal of Geophysical Research: Atmospheres*, *110*(D21).

(17) Zhang, X., Lin, Y. H., Surratt, J. D., & Weber, R. J. (2013). Sources, composition and absorption Ångstrom exponent of light-absorbing organic components in aerosol extracts from the Los Angeles Basin. *Environmental science & technology*, *47*(8), 3685-3693.

(18) Zhong, M., & Jang, M. (2014). Dynamic light absorption of biomass-burning organic carbon photochemically aged under natural sunlight. *Atmospheric Chemistry & Physics Discussions*, *14*(3).

(19) Chen, Y., Ge, X., Chen, H., Xie, X., Chen, Y., Wang, J., ... & Chen, M. (2018). Seasonal light absorption properties of water-soluble brown carbon in atmospheric fine particles in Nanjing, China. *Atmospheric Environment*, *187*, 230-240.

(20) Zhang, H., Wang, Z., Guo, P., & Wang, Z. (2009). A modeling study of the effects of direct radiative forcing due to carbonaceous aerosol on the climate in East Asia. *Advances in atmospheric sciences*, *26*(1), 57-66.

(21) Haywood, J., & Boucher, O. (2000). Estimates of the direct and indirect radiative forcing due to tropospheric aerosols: A review. *Reviews of geophysics*, *38*(4), 513-543.

(22) Zhang, Y., Forrister, H., Liu, J., Dibb, J., Anderson, B., Schwarz, J. P., ... & Weber, R. J. (2017). Top-of-atmosphere radiative forcing affected by brown carbon in the upper troposphere. *Nature Geoscience*, *10*(7), 486-489.

(23) Lin, G., Penner, J. E., Flanner, M. G., Sillman, S., Xu, L., & Zhou, C. (2014). Radiative forcing of organic aerosol in the atmosphere and on snow: Effects of SOA and brown carbon. *Journal of Geophysical Research: Atmospheres*, *119*(12), 7453-7476.

(24) Kampf, C. J., Filippi, A., Zuth, C., Hoffmann, T., & Opatz, T. (2016). Secondary brown carbon formation via the dicarbonyl imine pathway: nitrogen heterocycle formation and synergistic effects. *Physical Chemistry Chemical Physics*, *18*(27), 18353-18364.

(25) Updyke, K. M., Nguyen, T. B., & Nizkorodov, S. A. (2012). Formation of brown carbon via reactions of ammonia with secondary organic aerosols from biogenic and anthropogenic precursors. *Atmospheric environment*, *63*, 22-31.

(26) Sun, H., Biedermann, L., & Bond, T. C. (2007). Color of brown carbon: A model for ultraviolet and visible light absorption by organic carbon aerosol. *Geophysical Research Letters*, *34*(17).

(27) Aiona, P. K., Lee, H. J., Lin, P., Heller, F., Laskin, A., Laskin, J., & Nizkorodov, S. A. (2017). A role for 2-methyl pyrrole in the browning of 4-oxopentanal and limonene secondary organic aerosol. *Environmental science & technology*, *51*(19), 11048-11056.

(28) Amarnath, V., Anthony, D. C., Amarnath, K., Valentine, W. M., Wetterau, L. A., & Graham, D. G. (1991). Intermediates in the Paal-Knorr synthesis of pyrroles. *The Journal of Organic Chemistry*, *56*(24), 6924-6931.

(29) Nguyen, T. B., Laskin, A., Laskin, J., & Nizkorodov, S. A. (2013). Brown carbon formation from ketoaldehydes of biogenic monoterpenes. *Faraday discussions*, *165*, 473-494.

(30) Phillips, S. M., & Smith, G. D. (2014). Light absorption by charge transfer complexes in brown carbon aerosols. *Environmental Science & Technology Letters*, *1*(10), 382-386.

(31) Sasaki, S., Drummen, G. P., & Konishi, G. I. (2016). Recent advances in twisted intramolecular charge transfer (TICT) fluorescence and related phenomena in materials chemistry. *Journal of Materials Chemistry C*, *4*(14), 2731-2743.

(32) Rotkiewicz, K., Grellmann, K. H., & Grabowski, Z. R. (1973). Reinterpretation of the anomalous fluorescense of pn, n-dimethylamino-benzonitrile. *Chemical Physics Letters*, *19*(3), 315-318.

(33) Sarkar, A., & Chakravorti, S. (1995). A study on the spectroscopy and photophysics of N-phenyl pyrrole and N-phenyl pyrazole. *Chemical physics letters*, *235*(3-4), 195-201.

(34) Okuyama, K., Numata, Y., Odawara, S., & Suzuka, I. (1998). Electronic spectra of jet-cooled 1-phenylpyrrole: Large-amplitude torsional motion and twisted intramolecular charge-transfer phenomenon. *The Journal of chemical physics*, *109*(17), 7185-7196.

(35) Proppe, B., Merchán, M., & Serrano-Andrés, L. (2000). Theoretical study of the twisted intramolecular charge transfer in 1-phenylpyrrole. *The Journal of Physical Chemistry A*, *104*(7), 1608-1616.

(36) Rubio, M., Merchán, M., & Ortí, E. (1995). The internal rotational barrier of biphenyl studied with multiconfigurational second-order perturbation theory (CASPT2). *Theoretica chimica acta*, *91*(1), 17-29.

(37) Tsuzuki, S., & Tanabe, K. (1991). Ab initio molecular orbital calculations of the internal rotational potential of biphenyl using polarized basis sets with electron correlation correction. *The Journal of Physical Chemistry*, *95*(1), 139-144.

(38) Thomas, J. A., Young, J. W., Fleisher, A. J., Alvarez-Valtierra, L., & Pratt, D. W. (2010). Stark-Effect Studies of 1-Phenylpyrrole in the Gas Phase. Dipole Reversal upon Electronic Excitation. *The Journal of Physical Chemistry Letters*, *1*(13), 2017-2019.

(39) Schweke, D., Haas, Y., & Dick, B. (2005). Photophysics of phenylpyrrole derivatives and their acetonitrile clusters in the gas phase and in argon matrixes: Simulations of structure and reactivity. *The Journal of Physical Chemistry A*, *109*(17), 3830-3842.

(40) Baseden, K. A., & Tye, J. W. (2014). Introduction to density functional theory: calculations by hand on the helium atom. *Journal of Chemical Education*, *91*(12), 2116-2123.

(41) Chai, J. D., & Head-Gordon, M. (2008). Systematic optimization of long-range corrected hybrid density functionals. *The Journal of chemical physics*, *128*(8), 084106.

(42) Chai, J. D., & Head-Gordon, M. (2008). Long-range corrected hybrid density functionals with damped atom–atom dispersion corrections. *Physical Chemistry Chemical Physics*, *10*(44), 6615-6620.

(43) Krishnan, R. B. J. S., Binkley, J. S., Seeger, R., & Pople, J. A. (1980). Self-consistent molecular orbital methods. XX. A basis set for correlated wave functions. *The Journal of chemical physics*, *72*(1), 650-654.

(44) van Mourik, T., Bühl, M., & Gaigeot, M. P. (2014). Density functional theory across chemistry, physics and biology.

(45) Zhang, J., & Dolg, M. (2015). ABCluster: the artificial bee colony algorithm for cluster global optimization. *Physical Chemistry Chemical Physics*, *17*(37), 24173-24181.

(46) Zhang, J., & Dolg, M. (2016). Global optimization of clusters of rigid molecules using the artificial bee colony algorithm. *Physical Chemistry Chemical Physics*, *18*(4), 3003-3010.

(47) Smalley, R. E., Wharton, L., & Levy, D. H. (1977). Molecular optical spectroscopy with supersonic beams and jets. *Accounts of Chemical Research*, *10*(4), 139-145.

(48)Hayes, J. M., & Small, G. J. (1983). Supersonic jets, rotational cooling, and analytical chemistry. *Analytical Chemistry*, *55*(4), 565A-574A.

(49)Zwier, T. S. (2006). Laser probes of conformational isomerization in flexible molecules and complexes. *The Journal of Physical Chemistry A*, *110*(12), 4133-4150.

(50)Campargue, R. (1984). Progress in overexpanded supersonic jets and skimmed molecular beams in free-jet zones of silence. *The Journal of Physical Chemistry*, *88*(20), 4466-4474.

(51)Ullrich, S., Geppert, W. D., Dessent, C. E., & Müller-Dethlefs, K. (2000). Observation of rotational isomers I: A ZEKE and hole-burning spectroscopy study of 3-methoxyphenol. *The Journal of Physical Chemistry A*, *104*(51), 11864-11869.

(52)Fdez. Galván, I., Martín, M. E., Munoz-Losa, A., Sánchez, M. L., & Aguilar, M. A. (2011). Solvent effects on the structure and spectroscopy of the emitting states of 1-phenylpyrrole. *Journal of chemical theory and computation*, *7*(6), 1850-1857.

(53)Grabowski, Z. R., Rotkiewicz, K., & Rettig, W. (2003). Structural changes accompanying intramolecular electron transfer: focus on twisted intramolecular charge-transfer states and structures. *Chemical reviews*, *103*(10), 3899-4032.
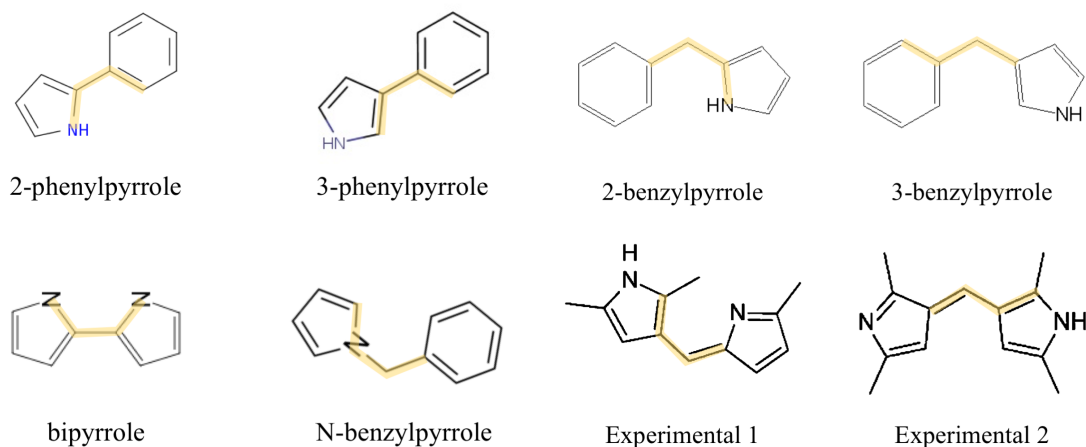
Appendix

2-phenylpyrrole   3-phenylpyrrole   2-benzylpyrrole   3-benzylpyrrole

bipyrrole   N-benzylpyrrole   Experimental 1   Experimental 2

Figure S1: The structures of the additional pyrrole molecules studied by computational methods and the dihedral angle of interest measured.

Table S1: The optimized ground and excited state information for the other pyrrole derivatives studied using computational methods for the bare chromophore.

Molecule	Unique Conformer Number	Excited State Relative Energy (cm^{-1})	Ground State Dihedral	Excited State Dihedral
Bipyrrole	1	32793.2408	46.04446	0.00795
	2	34101.52906	-148.29444	-170.70155
Experimental 1	1	24723.59764	18.86932	73.85738
	2	24870.2065	-40.92001	-27.07744
Experimental 2	1	15300.4547	-51.93458	1.57344
	2	19757.7641	-170.40587	10.65168
Nbenzylpyrrole	1	41397.9627	84.97825	83.97372
3benzylpyrrole	1	40775.97218	88.75643	-0.01766
	2	41291.29878	-146.48396	-141.46534
	3	41291.7373	-146.47506	-141.46341
3phenylpyrrole	1	36498.63096	31.79706	0.0016
	2	36497.3141	31.77681	0.00375
2phenylpyrrole	1	33923.53514	-30.00915	-2.36825
	2	33919.14564	-29.97417	-2.3678

Table S2: The optimized ground and excited state information for the other pyrrole derivatives studied using computational methods for 1PhPy + 1H$_2$O.

Molecule	Unique Conformer Number	Excited State Relative Energy (cm^{-1})	Ground State Dihedral	Excited State Dihedral
Bipyrrole	1	33577.204	-23.26463	-0.38051
Nbenzylpyrrole	1	41688.98649	85.50227	87.81301
2benzylpyrrole	1	35794.117	77.29018	70.03451
3benzylpyrrole	2	37397.37944	-96.58757	-93.33437
3phenylpyrrole	1	34644.729	31.36272	3.23761
2phenylpyrrole	1	33530.8954	-28.8017	-4.81926

Table S3: The optimized ground and excited state information for the other pyrrole derivatives studied using computational methods for 1PhPy + 2H$_2$O.

Molecule	Unique Conformer Number	Excited State Relative Energy (cm^{-1})	Ground State Dihedral	Excited State Dihedral
Bipyrrole	1	34630.243	135.18879	179.99721
	2	34637.7055	135.36618	179.95909
Experimental 1	1	22427.674	36.78783	76.64447
	2	25503.391	-38.69408	-74.88328
Nbenzylpyrrole	1	41571.12862	46.38094	51.22331
2benzylpyrrole	1	36024.7848	-51.11025	-21.13583
3benzylpyrrole	1	38667.699	95.89218	92.22219
	2	39201.2415	-95.93006	117.00051
3phenylpyrrole	1	35822.2105	30.31611	0.02208
2phenylpyrrole	1	33669.1637	36.82932	12.19126

Table S4: The optimized ground and excited state information for the other pyrrole derivatives studied using computational methods for 1PhPy + 3H$_2$O.

Molecule	Unique Conformer Number	Excited State Relative Energy (cm^{-1})	Ground State Dihedral	Excited State Dihedral
Bipyrrole	1	33040.3695	34.33204	0.009
	2	32849.2065	-33.78302	-0.00237
Nbenzylpyrrole	1	41710.714	144.50243	-38.1277
2benzylpyrrole	1	36809.72667	-73.1002	-66.90516
3benzylpyrrole	2	37223.117	-93.75713	-60.0235
3phenylpyrrole	1	34652.62985	30.91075	-1.65898
2phenylpyrrole	1	33376.823	-33.48514	-13.70595